Université de Neuchâtel
Institut de Microtechnique

# The study of bistable GaAs Fabry-Perot devices for operation in array format

## Thèse

Présentée à la Faculté des sciences
pour obtenir le grade de docteur ès sciences

par

Christophe Bagnoud

Neuchâtel, décembre 1993

# IMPRIMATUR POUR LA THÈSE

The study of bistable GaAs Fabry-Perot devices for operation in array format

de Monsieur Christophe Bagnoud

---

UNIVERSITÉ DE NEUCHÂTEL

FACULTÉ DES SCIENCES

La Faculté des sciences de l'Université de Neuchâtel
sur le rapport des membres du jury,
Messieurs R. Dändliker, A. Shah, B.S. Wherrett (Edinburgh) et J.-L. Oudar (Bagneux)

autorise l'impression de la présente thèse.

Neuchâtel, le 31 décembre 1993

Le doyen :

H.-H. Nägeli

# Abstract

An integrated nonlinear Fabry-Perot device (NLFP) is presented. It consists of a 2 μm bulk GaAs spacer sandwiched between two AlGaAs dielectric mirrors. This device exhibits optical bistability and it has potential applications as an all-optical logic gate or memory.

The NLFP shows thermally stable bistable switching with a high contrast and a threshold power in the order of 1 mW for an optimum spotsize of 6 μm. A switching energy of 15 pJ is derived from critical slowing down measurements. Optical bistability is observed at wavelengths between 853 and 890 nm using the same NLFP sample. The threshold power is highly sensitive to the operating wavelength.

Towards system applications, we distinguish between two-port and three-port operation of the NLFP. Both types of operation are investigated and their characteristics are studied. A high differential gain (5 to 7) is measured for both two- and three-port operation. We confirmed experimentally that an off-axis addressing of the signal beam is favorable and can improve the achievable differential gain by a factor of two. The NLFP is tested for cascadability. The beam reflected from the device is delayed by 260 ns with a monomode fiber and used as on-axis signal beam on the same device. The cascadable operation is demonstrated by a repetitive switching of the NLFP from high to low reflectivity state for every second delayed pulse. The operation is limited by the gain-bandwidth product of 100 MHz.

The behavior of the device in array format is studied. The minimum separation between the devices for negligible crosstalk is determined. A Dammann grating is used to generate a 3x5 array of spots, which are 6 μm large (minimum threshold) and 50 μm separated (negligible crosstalk). The switching characteristics of the NLFP in array format is investigated accurately using a CCD-camera and a 2x2 array of fast detectors. We conclude from the measurements, that the homogeneity of the sample limits the threshold power uniformity across the array to about ±5 %. This threshold power nonuniformity

will complicate the use of the NLFP as a parallel processing element in an advanced cascadable system.

# Table of contents

# 1 Introduction

The first observation of passive nonthermal optical bistability based on electronic nonlinearity was made in a bulk GaAs device at low temperature in 1979 by Gibbs et al. [2]. The same effect was observed at room temperature in 1982 [3]. Since these observations, the GaAs etalons have stimulated a considerable interest in the fields of telecommunication, signal processing and computing.

The optical bistable device in this thesis is similar in concept to the device first studied by Gibbs. It has a structure which consists of a nonlinear spacer of bulk GaAs sandwiched between two integrated AlGaAs mirrors. We shall refer to it as the nonlinear Fabry-Perot device (NLFP). The complete device can now be made in one epitaxial growth. The device we have used shows low threshold for switch-On (1 mW) with high contrast (8:1) [4]. It demonstrates thermally stable operation over a period of approximately 500 ms [5].

However, there are some limitations in the potential application of this NLFP which are due to the material, on the one hand, and the structure, on the other hand. The reset of the device from On- to Off-state is limited by the lifetime of the carriers in the cavity to 4 to 10 nanoseconds. This limits the overall operating speed to a speed comparable with present-day electronics. Moreover, the structure of the NLFP also limits the full exploitation of the parallelism capability offered by optics. The number of signal beams with the same wavelength and polarization which can be accepted by the device (fan-in) is limited by the angular acceptance of the resonator structure to about 2 [1]. This limits the range of architectures to digital ones.

In the digital domain, the numbers are represented in a binary system and the operations are logic operations. The input-output characteristics of the NLFP is, as we will see, well suited for these types of operations. The NLFP is either in high reflectivity state (Off-state, "one") below threshold or in low reflectivity state (On-state, "zero") above threshold. The key to using this device in digital optics

is the potential for operating a large array of similar devices in parallel. Used in this way, the NLFP can compensate the limitation of speed mentioned earlier.

In this thesis, we want first to assess the potentialities of the NLFP as a device for advanced all optical systems, and second to evaluate its potentialities in a small array format.

The text is organized as follows : In the following chapter, the first main part introduces the structure of the nonlinear Fabry-Perot (NLFP) and outlines the critical points with respect to its growth and to the nonlinear characteristics required. The second part introduces the characterization techniques used; presents the investigated samples; and summarizes the linear and nonlinear measurements on the elements. Chapter 3 assesses the potentialities of the NLFP as an element for optical computing. The requirements and modes of operation to use this optical switch in a system are clearly established. The different possibilities to input the hold beam and the signals are evaluated. Cascadable operations are demonstrated. In Chapter 4, an array of 3x5 NLFPs is investigated. First, the spacing between devices for minimum crosstalk is evaluated. Then, the setup for array operation is described. Measurements of the threshold uniformity in the array are presented and compared with single spot measurements in the last part.

Note :

This thesis work was conducted within the framework of a project of the Swiss National Science Foundation. It is partially the result of a fruitful collaboration with Bruno Acklin. Most of the results of this period of collaboration are contained in his thesis work published in 1992 at the University of Neuchâtel [1] and in some publications cited in the following. The Chapter 2 contents essentially the summary of the published results which are important for the following chapters, and the characterization of the two samples which were grown after Acklin's departure (Sample #467 and #487).

# 2 Device and basic measurements

The aim of this chapter is to present the Nonlinear Fabry-Perot device (NLFP) outlining its basic characteristics. The first part will describe shortly its structure and the basic nonlinear optical characteristics of the spacer to the incoming light. Basic equations describing the NLFP characteristics and its bistable behavior will be summarized and the critical aspects for the epitaxial growth of the device will be specified. In the second part, the experimental setup used for linear and nonlinear measurements will be described. Then each sample will be introduced and its linear characteristics described. Measurements on optical bistability will be presented finally.

## 2.1 Structure of the NLFP

The NLFP device can demonstrate bistable features : It has the capability to show two distinct and stable output states for one input. The output states depend only on the history of the input. This interesting feature opens the door to many important possibilities for its utilization in the domain of photonic switching as switch, memory, logic gate etc.

The principle of optical bistability requires two features : the nonlinearity and the feedback. As material providing a large nonlinearity we choose bulk GaAs. We use mirrors as a means of internal optical feedback by introducing the nonlinear material in a resonator (= a resonant optical cavity).

Intrinsic optical bistability is a well-known principle based here on the control of the refractive index by the internal light intensity in the resonator; it is treated extensively in ref. [1]. Here we want to treat what motivates our choices on the resonant optical nonlinearity and the structure, and also to introduce the necessary concepts and formulas which are used for the following work.

## 2.1.1 Basic theory

The choice of the nonlinear material is the most determining factor for the future characteristics of the bistable device. Some direct-gap semiconductors exhibit large optical nonlinearities (GaAs, CdS, InSb, ZnSe). These large effects are in GaAs a consequence of a resonant coupling to the bandgap, and will lead to low power switching devices with low response time.

GaAs is one of the most promising materials to date. Its gap energy $E_g$ is situated at 1.424 eV, close to where arrays of sources exist and arrays of Si-detectors which can be used at high detection sensitivity in this spectral domain. Crystal qualities are well known as a consequence of the widely distributed technology (as example, GaAs ICs with complexities up to ~ 1000 components/chip have been constructed already in 1984, and also the integration of electronic and photonic devices on a single GaAs substrate [6]). A NLFP device, consisting of a bulk GaAs layer sandwiched between two dielectric mirrors in $Al_xGa_{1-x}As$ can be grown on a GaAs substrate in a single epitaxial process.

Compared to multiple quantum well (MQW) GaAs NLFP structures [7], where the excitonic features are enhanced by the confinement, structures in GaAs bulk of similar finesse show comparable threshold. Excitons in MQW material saturate below the critical intensities necessary for bistability, therefore the bistable effect relies on the same nonlinear material contributions as for the bulk NLFP [8]. We can define a phenomenological Kerr coefficient $n_2 \equiv \delta n/\delta I$, where $\delta I$ is the change in the internal intensity in the cavity. The value of this coefficient is comparable in both MQW and bulk materials, but with a slight advantage for bulk (2.2.4)[1]. Moreover, the bulk GaAs NLFP is cheaper and easier to grow in large production than MQW devices.

OPTICAL CHARACTERISTICS OF GaAs

The nonlinear effect in GaAs is carrier dependent. A change in the internal cavity intensity I produces a linear change in the free carrier density $\Delta N$ (if the absorption $\alpha$ is small). This induces a proportional refractive index change $\Delta n \approx n_2 I$, where $n_2$ is a phenomenological

Kerr coefficient which characterizes the material. We consider here time scales larger than the intraband carrier recombination time τ (4-10 ns) and a nearly constant absorption α. Then

$$n(I) = n + n_2 I \quad \text{with} \quad n_2 = \eta \frac{\tau \alpha}{\hbar \omega}, \tag{2-1}$$

where $\hbar\omega$ is the photon energy, α is the linear absorption coefficient, and $\eta$ is defined as a constant nonlinear refractive cross-section $\eta = \delta n/\delta N$. N is the (ambipolar) carrier density, which is related to the internal intensity by the carrier rate equation [9]

$$\frac{dN}{dt} = \frac{\alpha(\omega,N)I}{\hbar\omega} - \frac{N - N_{te}}{\tau}. \tag{2-2}$$

$N_{te}$ is the density of electron and hole pairs at thermal equilibrium. In the steady-state, the change of carrier density dN/dt can be set to 0. The optical properties $\alpha(\omega,N)$ and $\Delta n(\omega,N)$ can be interpolated from published experimental data (Fig. 2-1) [10]. By comparing these measurements with the plasma theory [11], it can be determined that plasma screening of the Coulomb enhancement of continuum states and band filling are the dominant contributions to the dispersive nonlinearity in GaAs. Plasma theory is a model which gives an analytical expression for the density dependent absorption spectrum in GaAs, from which the corresponding nonlinear refractive index change can be calculated using a Kramers-Kronig transform. The maximal dispersive change is found below the fundamental absorption edge, where absorption is low. The large residual absorption found in the experimental measurements below the gap is represented for our design calculations by an exponential bandtail. The dispersion curve for the linear refractive index of GaAs is given in ref. [12].

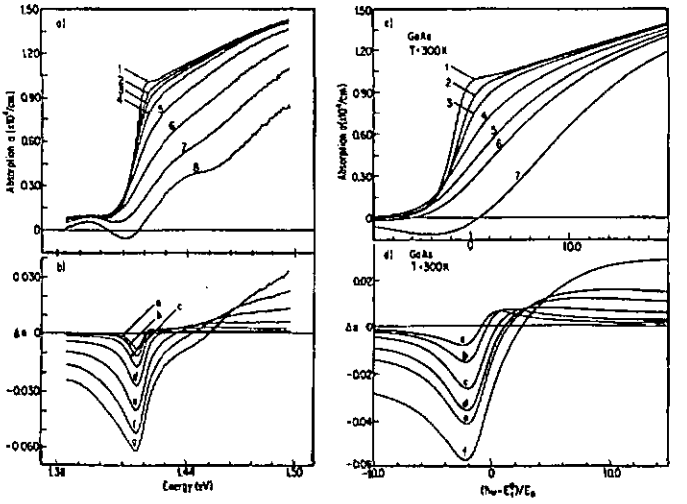

*Fig. 2-1 Experimental (left) and theoretical (right) absorption and refractive index changes are compared for room temperature GaAs [10].*
*a) Measured absorption (curves 1-8) on a 15 μm spotsize at 0, 0.2, 0.5, 1.3, 3.2, 8, 20, 50 mW power.*
*c) Calculated absorption spectra (curves 1-7) for different electron-hole pair densities N=0.001, 0.08, 0.2, 0.5, 0.8, 1 and $1.5 \cdot 10^{18}$ $cm^{-3}$ (plasma theory).*
*b) and d) : Refractive index changes corresponding to a) and b) obtained through Kramers-Kronig transformation.*

MIRRORS : PERIODIC LAYERED STRUCTURES

Two dielectric Bragg-reflectors enclose the nonlinear layer. They are formed by $\lambda/4$-$Al_xGa_{1-x}As$ stacks of alternating high and low refractive indices by changing the Al concentration x [13]. The Bragg wavelength $\lambda_B$ must be set to the working wavelength to ensure maximal reflectivity and to avoid undesired phase contributions, namely

$$n_H d_H = n_L d_L = \frac{\lambda_B}{4}. \qquad (2\text{-}3)$$

The maximum spectral width for the stopband of the mirror is obtained by maximizing the difference between $n_H$ and $n_L$. Therefore the low index layer will consist of pure AlAs. (It was necessary to add a monolayer of GaAs every 100 Å in these $\lambda/4$ stacks to improve the surface quality on the two first samples of the four concerning this work.) The high refractive index layer, with an Al concentration of $x = 0.07$, shows a bandgap below 820 nm, which gives an absorption in the stack of less than 10 $cm^{-1}$. Typical spectral width of the mirror stopband is larger than 100 nm. A typical reflectivity spectra of the rear mirror of a NLFP (#476, Sect. 2.2.2) could be measured after etching of the front mirror and the spacer layer (Fig. 2-2). The Bragg wavelength was found at 887 nm and the spectral width of the stopband was determined as 103 nm. Discrepancy of this spectral width with the calculated (115 nm) is caused by the accidental etching of ≈ 60 % of the first $\lambda/4$ stack of the mirror.

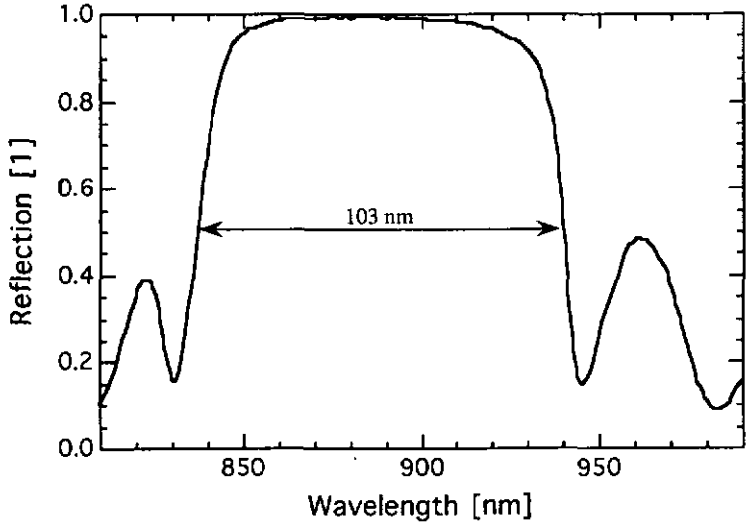


*Fig. 2-2 Spectral reflectivity measurement of the stopband of the rear mirror of sample #476.*

The NLFP will be used in reflection, profiting from the multiple advantages of this mode of utilization over the transmission mode listed by Wherrett [14].

The rear mirror reflectivity has to be set as high as possible to avoid losses in the substrate. The front mirror reflectivity must be finely adjusted. Mirror characteristics can be calculated using the numerical simulation tool or using a coupled wave theory [1].

## 2.1.2 Design features and related formulae

Table 1.1 summarizes the important formulae for the design of the NLFP. This is divided into : a) a part describing the Fabry-Perot parameters; b) basic mathematical relations, and c) the bistability formulae. Some important features of the design are described below.

DESIGN FEATURES

The design of the NLFP was conducted towards low threshold power for the optical bistability and high switching contrast. Fine tuning on the design was accomplished by using a numerical tool (NLB) developed at IMT and EPFL/IMO, which can simulate the frequency and intensity dependent response of nonlinear layered structures to plane wave illumination [1]. Carrier dependent nonlinear refractive indices in each layer are obtained by iterating self-consistently the carrier equation (2-2) using published experimental data for $\alpha(\omega,N)$ and $\Delta n(\omega,N)$ [10]. Before the optimization, a preliminary design must be proposed.

First, the resonance wavelength must be chosen. This initial guess is not extremely critical as optical bistability can be observed over a large wavelength range up to 890 nm above the gap wavelength. Experiences on previous devices helped in this choice for the later structures.

The spacer length can then be adapted; this choice can be directed towards low threshold or low wavelength sensitivity. The threshold power can be decreased by increasing the cavity finesse (Eq. (2-16)). This finesse increases inversely proportional to the losses in the cavity. Therefore, a low threshold power can be obtained by designing a short spacer device. But the simulations show that the wavelength sensitivity of the device increases with finesse.

In a third step, the front mirror reflectivity is determined according to the impedance matching condition.

IMPEDANCE MATCHING CONDITION

The switching contrast C is defined as the ratio of the reflectivity before switching ($R_{Off}$) and the reflectivity after switching ($R_{On}$). This value can be increased towards infinity with a vanishing reflectivity in the On-state, by choosing the front mirror reflectivity such that

$$R_f = R_b(1-A_f)^2 e^{-2\alpha L}, \qquad (2\text{-}4)$$

where $R_f$ and $R_b$ describe the front and back reflectivity respectively, $A_f$ the losses in the front mirror (less than 0.05 %) and L the spacer length. This condition is called impedance matching (IM). As the necessary spectral detuning from the resonance minimum for bistability must be about one FWHM, the Off-resonance reflectivity is in this case close to maximum.

FORMULAE

**a ) NLFP parameters**

| | |
|---|---|
| $R_f$, $R_b$ | Front resp. back mirror reflectivity |
| $A_f$ | Front mirror absorption |
| $\rho_f \equiv \frac{R_f}{1-A_f}$ | Normalized front mirror reflectivity |
| $\Phi_m$ | Phase-shift in the two dielectric mirrors |
| $L_m \equiv \frac{1}{2n}\frac{\delta(\Phi_m)}{\delta k}$ | Equivalent length of the mirrors |
| L | Spacer length |
| $L_{eff} = L + L_m$ | Effective length |
| n | Refractive index of the spacer |

| | |
|---|---|
| $n_g \equiv n - \frac{\delta n}{\delta \lambda}\lambda$ | Refractive index in presence of dispersion |
| $\Delta\varphi_{fsr} = \pi$ | Free spectral range |
| $\delta\varphi$ | FWHM of the resonance |
| $\xi \equiv \frac{\hbar c}{\eta \tau}$ | Material parameter |

## b ) NLFP equations

| | | |
|---|---|---|
| $2\varphi = 2knL + \Phi_m$ | Cavity round-trip phase | (2-5) |
| $2\varphi_q = 2\pi \cdot q$ | Resonance condition (of q-order) | (2-6) |
| $\rho = \sqrt{R_f R_b} e^{-\alpha L}$ | Round trip attenuation of the field | (2-7) |
| $\mathrm{F} \equiv \frac{\Delta\varphi_{\mathrm{fsr}}}{\delta\varphi} = \frac{\pi\sqrt{\rho}}{1-\rho}$ | Finesse | (2-8) |
| $T_{FP}(\varphi) = \left[1 + \left(\frac{2\mathrm{F}}{\pi}\right)^2 \sin^2\varphi\right]^{-1}$ | Airy function (transmission of the ideal FP) | (2-9) |
| $R = (1-A_f)\left[1 - T_{FP}(\varphi)\frac{(1-\rho_f)(1-\rho^2/\rho_f)}{(1-\rho^2)}\right] \equiv \left[1 - T_{FP}(\varphi)(1-R_{\min})\right]$ | Reflection of the Fabry-Perot | (2-10) |
| $\Delta\lambda_{fsr} = \frac{\lambda^2}{2n_g L}$ | Free spectral range (expressed in wavelength) | (2-11) |

## c ) Optical bistability

(HFA means "in the limit of the High Finesse Approximation" i.e. F > 10.)

| | | |
|---|---|---|
| $T_f \approx 2\alpha L$ | Impedance match (HFA) | (2-12) |
| $\mathrm{F} \approx \frac{\pi}{2\alpha L}$ | Finesse of the FP (HFA) | (2-13) |
| $I_i$ | Incident intensity | |

| | | |
|---|---|---|
| $I(\varphi) \approx I_i \frac{2F}{\pi} T_{FP}(\varphi) \approx I_i \frac{2F}{\pi} \left( 1 + \left( \frac{2F}{\pi} \right)^2 \varphi^2 \right)^{-1}$ | Spatially averaged cavity intensity (HFA) | (2-14) |
| $\varphi_0{}^c = \sqrt{3} \frac{\pi}{2F}$ | Critical cavity detuning for bistability (HFA) | (2-15) |
| $I_i{}^c = \frac{8\pi}{3\sqrt{3}} \frac{\xi}{2F}$ | Minimum threshold intensity for bistable switching (HFA) | (2-16) |

*Table 1.1 Summary of some useful formulae for the NLFP and its bistable features. a) Fabry-Perot parameters, b) basic equations of the NLFP and c) characteristics relations or calculations for bistability. These formulae are developed in ref. [1].*

## 2.1.3 Critical aspects in the device

All the structures were grown by Molecular Beam Epitaxy (MBE, Varian) at the Institut de Micro- et Optoélectronique (IMO) of the Ecole Polytechnique Fédérale in Lausanne (EPFL).

Success of the last sample described in this work (NLFP #487) is mainly due to the fact that an optical characterization of the previous sample (NLFP #476) was done quickly, allowing us to determine the growth parameters, in particular the growth rate of the spacer. Then the results of the characterization were communicated to the crystal growers. A regrowth with comparable parameters could be completed shortly afterwards in order to achieve the required spacer length accuracy.

We can use temperature tuning to adjust the absorption in a spacer with a non-accurate length to achieve bistability if the device is not bistable at room temperature or to reduce the threshold power. It is shown in the following (2.2.2) that it was possible with this means to reduce the threshold power of a sample with a spacer layer of 1.9 % too short (sample #476) from 3.3 mW at room temperature to 1.6 mW at 0°. We observed an improvement of the contrast at the same time. This means is limited to small adjustments because a shift of the resonance wavelength caused by the thermal refractive index change

arises in parallel to the shift of the absorption and reduces its effect [1].

SPACER LENGTH ACCURACY

This is the most critical requirement of the NLFP device. The relative error $\Delta L/L$ for the nonlinear spacer must be controlled better than 0.5 % to ensure a precision of ± 3 nm on the designed resonance wavelength (we measured 12 % threshold increase from 883 to 888 nm on sample #487). This means that a precision better than ±10 nm is required for the 2 µm GaAs spacer NLFP that we will use here. As the MBE apparatus shows an accuracy of 1 - 2 %, this requirement is very demanding.

The design wavelength is chosen at 885 nm, which is the average of a range of wavelengths where the threshold is minimum. If the spacer is thinner, then the wavelength of the resonance decreases and the high exponential increase of the absorption near the band-edge will remove the NLFP from the impedance match condition. If the spacer is larger, then the resonance wavelength increases and the diminishing absorption will induce less critical changes for the impedance matching of the device. Moreover, if the spacer is larger, the desired absorption can be recovered by heating the sample. The absorption is not known with enough spectral accuracy for a precise design. The absorption data measured by Lee (Fig. 2-1) are shifted by + 3 nm from those that we determine from the finesse of the device (Eq. (2-13)).

ACCURACY IN THE PERIODS OF THE MIRROR STACKS

An error in the period of the mirror stacks will be followed by two consequences. The first consequence is a change in the penetration depth in the mirrors by an additional (linear) phase contribution, which causes a wavelength shift of the resonance. The wavelength tolerance of 3 nm set before will limit here the acceptable relative error of the stack period to 1.3 % [1]. The second consequence is the change in reflectivity of the dielectric mirror and is negligible for wavelength changes of 3 nm (the spectral width of the stopband of the mirrors is larger than 100 nm). A detuning of the Bragg wavelength of the rear mirror was measured as 3 % towards short wavelength in

the first sample (#337), impeding the bistability, and as 5 % towards long wavelength for the second one (#360). The rear mirrors of the two last samples (#476 and #487) were correctly centered spectrally (Fig. 2-2).

ERRORS IN IMPEDANCE MATCH

As a consequence of the errors above listed, the IM-condition may not be fulfilled if the resonance is spectrally shifted. This leads to a loss of contrast. But it can be derived from Eq. (2-10) that the minimum reflectivity of the NLFP depends quadratically on deviation of the spacer length [1].

## 2.2 Linear and nonlinear behavior of the NLFP

### 2.2.1 Principal measurements

LINEAR AND NONLINEAR MEASUREMENT SETUP

Linear ($P < 100\ \mu W$) and nonlinear measurements can be conducted with the same experimental setup shown in Fig. 2-3. Using the same coherent light source at a fixed wavelength and with an increasing intensity, we can measure the switching characteristic with fast detectors. First, the parts of the setup will be described, and second, the possible measurements relevant for the following work will be presented.

The setup allows reflectivity measurements using a diffraction limited spot with a spectral resolution better than 0.1 nm together with a SNR of 25 dB. Bistability measurements can be made at the same place with a bandwidth up to 25 MHz.

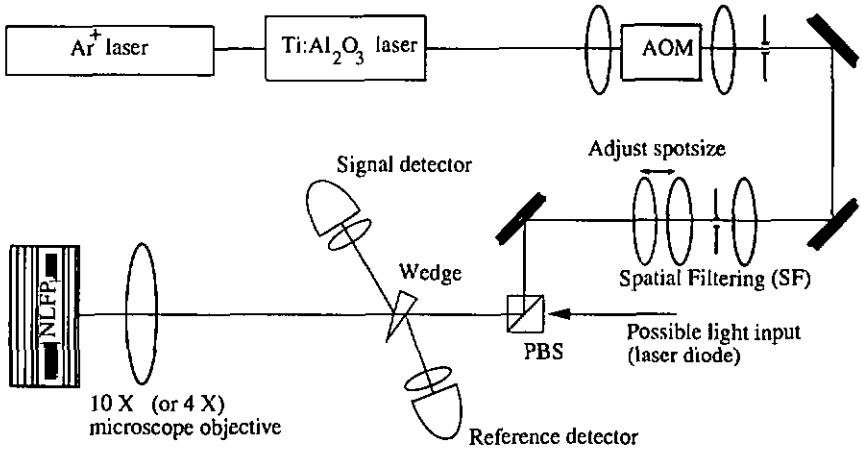


*Fig. 2-3 Experimental setup used for linear and nonlinear measurements.*

The light source is a Titanium-Sapphire laser (Coherent CR-899) pumped by a 8 W Argon laser (Coherent CR-599). Typical output power at 885 nm is at 600 mW. The specified linewidth of the $Ti:Al_2O_3$ laser is < 2 GHz. The maximum intensity noise is of the order of 3 %. The laser has been equipped with a stepper-motor to allow computer controlled wavelength tuning in 0.2 Å steps. Usable output wavelength range is from 780 to 950 nm. A 5 W $Ar^+$-pumped dye laser using Styril 9 M dye was used previously.

The short pulse generation is performed by means of an acousto-optic modulator (Automates et Automatismes MP-10, acoustic carrier frequency of 200 MHz) driven by a 50 MHz pulse generator (Phillips PM 5715 or HP 8112A). The pulse generator is placed in a telescopic setup with two f = 60 mm lenses (which can be replaced by two f = 35 mm lenses for faster pulse rise times), which allows the generation of 15 ns rise time pulses. The efficiency in the first order is about 70 % and the zero-order suppression is 35 dB. In normal utilization, we use pulses of 1 μs duration with a repetition rate of 10 kHz.

A spatial filter (SF) placed after the acousto-optic modulator (AOM) produces a collimated beam which is focused by the 10X microscope objective on a 6 μm diameter spot. By moving the second lens of the

SF, this spotsize can be adapted on the sample from 4 to 40 μm. The spotsize was determined by measuring the far-field diffraction angle of the Gaussian beam.

The sample holder allows the sample positioning in x-, y- and z-direction with a 5 μm repositioning accuracy. Positioning in x- and y-direction are equipped with two stepper-motor for computer- or manual-controlled motion. The sample is placed on a 2.6 W Peltier-cooler which allows an electronic temperature control with a temperature stability better than 1 K.

The sample holder can be replaced by a home built $N_2$-cryostat for a wider temperature range from - 170 to 170 °C with a temperature stability of 0.1 K.

The signal detection is possible by using reflections from an uncoated glass wedge and focusing them on the fast reference and signal detectors (Analog Modules 712A-3-B). The sensitivity of the detectors is 40 V/mW with a bandwidth of 40 MHz at a bias voltage of 60 V.

## SPECTRAL REFLECTIVITY MEASUREMENTS (SRM)

### Linear measurements

Spectral reflectivity measurements at very low intensity (≈ 35 μW) can be achieved by using lock-in detection of the pulsed signal and reference. The output of the two lock-in amplifiers (Stanford Research SR530) is digitalized by a data acquisition card (Metrabyte DASH-16G). Data acquisition and wavelength change are conducted by computer. Reflectivity calibration was accomplished by means of an uncoated gold mirror (Balzers).

The relevant optical properties of the device can be measured. Resonance wavelength and reflectivity minimum are directly readable from the reflectivity spectrum and information on the mirror characteristics and the absorption in the spacer can be deduced. The spectra can be directly compared with those given by the simulation (e.g. Fig. 2-8). By this comparison according to spacer length variations in the simulation, this value can be determined with an accuracy of ± 1 % for the device. The spectral resolution of $\Delta\lambda = 0.3$ nm is given by the resolution in wavelength allowed by the

diffraction limited Gaussian spot of 6 μm. This resolution can be improved to 0.05 nm by enlarging the spot diameter to 15 μm.

**Nonlinear measurements**

Nonlinear spectral reflectivity measurements can be achieved by using the same process, also with the lock-in detection (but with attenuation of the signals before lock-in for linearity) and by varying the intensity of the incident pulses. To avoid heating, pulses with 1 μs duration and a duty cycle of 1 % were used [15].

DYNAMIC SWITCHING MEASUREMENTS

Threshold power, contrast, differential reflectivity changes and hysteresis width can be determined for a given wavelength by measuring the output of the reference and the signal detectors on the oscilloscope (HP 54504A, 400 MHz, 200 Msample/s).

## 2.2.2 Investigated samples

All the investigated samples have the same spacer material (undoped bulk GaAs). The spacer length is the same (1.96 μm = 16λ/2n) for three structures (except #337), which are designed for a working wavelength of 885 nm where the measured absorption is ≈ 240 $cm^{-1}$ [1]. The front mirror reflectivity is 0.91 (7 λ/2-stacks) following the IM-condition. The back mirror reflectivity of ≈ 1 is obtained with 19.5 λ/2-stacks. Sample #337 (1.95 μm spacer length) is the precursor device of the series, and it is dimensioned for a working wavelength of 882 nm, but otherwise the structure is comparable with the others (only 5 λ/2-stacks for the front mirror).

We decided to concentrate our measurements on the basic structure of the three last devices for the principal reason that, since it is designed for application in array format, the structure presents low wavelength sensitivity rather than very low threshold. Simulations showed that the threshold power change according to the wavelength detuning from resonance was more critical for short spacer devices [1] than for longer ones. A choice of a 2 μm spacer with one milliwatt threshold was favorable according to this argument. The encouraging results obtained with sample #360 led us in this direction. Moreover,

the growth accuracy is approximately the same for a 2 μm spacer than for a much shorter one but more accuracy is required for the mirrors in the case of thinner spacer.

BASIC STRUCTURE

The layout of the basic structure as it was proposed for #360 [1] is sketched in Fig. 2-4. The layout for the three other structures differ only by small details from it. The mirrors are doped p and n from top to bottom with $10^{18}$ to $10^{17}$ $cm^{-3}$ Be (p) and with $10^{17}$ to $10^{18}$ $cm^{-3}$ Si (n) for the front and back mirror respectively. The spacer layer is formed of intrinsic bulk GaAs.

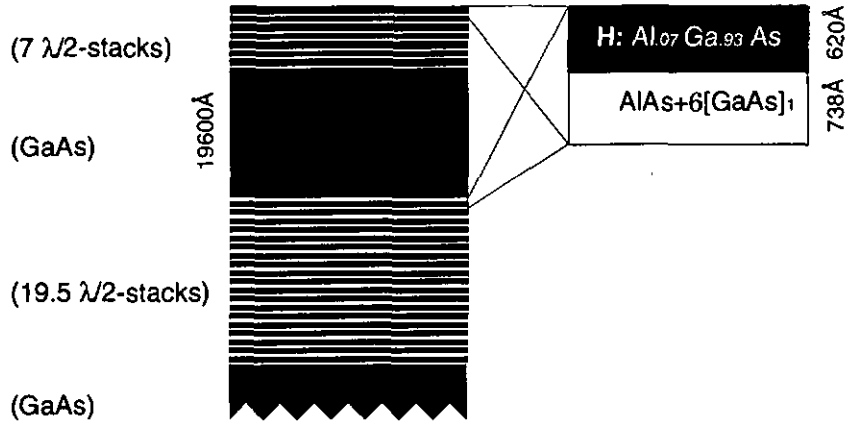


*Fig. 2-4 Basic structure (layout for #360). The order of resonance in the spacer is q = 16 (L = 16 λ/2n).*

The bistable characteristics for this structure predicted by the numerical simulation are shown in Fig. 2-5.

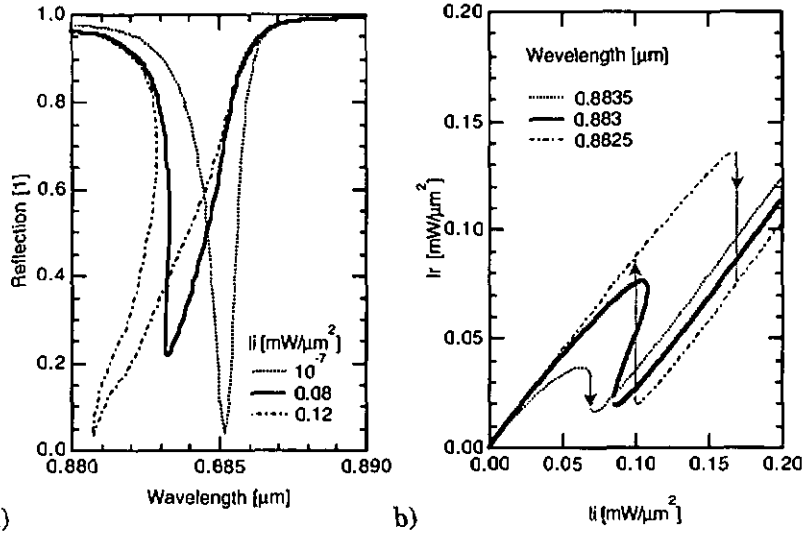


*Fig. 2-5* *Simulation of the bistable characteristics of the basic structure.*
*a) Reflectivity of the device vs. wavelength for three different incident intensities ($10^{-7}$, 0.08 and 0.12 mW/µm²). 0.08 mW/µm² is approximately the minimal threshold intensity.*
*b)Reflected vs. incident intensity at different detuning wavelengths ($\lambda_{res}$=885.2 nm). Minimal threshold wavelength is ≈ 883.5 nm.*

SAMPLE #337

This NLFP differs from the basic structure (Fig. 2-4) by having only 5 λ/2-stacks in the front mirror, 18.5 λ/2-stacks in the back mirror and a spacer length of 1.95 µm. The reasons for these discrepancies are that this first device was optimized for a resonance wavelength of 882 nm, and the estimated absorption of $\alpha \approx 600\ cm^{-1}$ at this wavelength leads to a predicted reflectivity for the front mirror of ≈ 75 % to satisfy the IM condition. As another difference, the high refractive index λ/4-stack has been grown as a superlattice of AlAs/GaAs ($[GaAs]_8[AlAs]_3$) because only one Al-source was available at that time in the MBE.

The structure of sample #337, observed with a transmission electron microscope, is shown in Fig. 2-6 a). A thickness measurement of ± 5% is achieved with this method. A typical linear spectral reflectivity measurement (SRM) of this sample is given in Fig. 2-6 b), showing a resonance wavelength of 882 nm with a FWHM of 2.8 nm. The finesse of the FP was about 11. (This measurement was performed with the dye laser and a Styril 9M dye.)

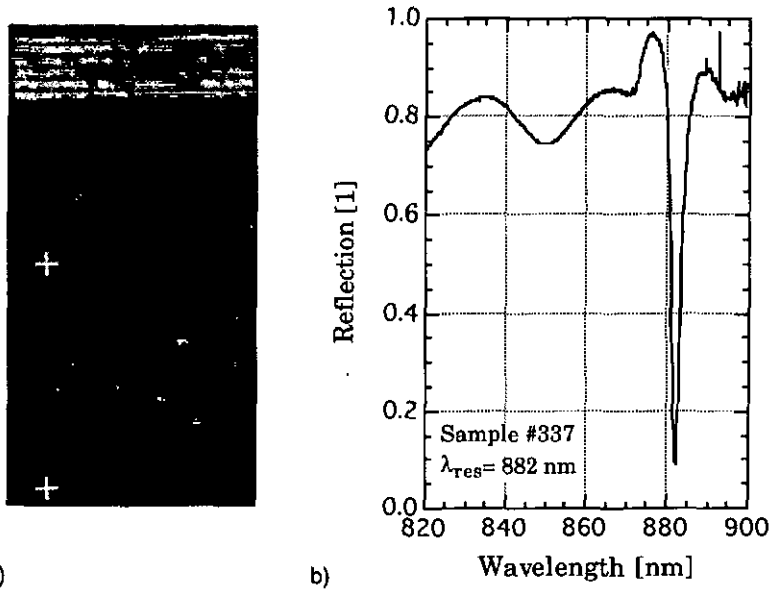


*Fig. 2-6* *a) TEM picture of sample #337 showing the structure of a 1.95 μm spacer sandwiched between two Bragg-mirrors of 5 and 18.5 half-wave dielectric stacks. The distance delimited by the markers is measured as 2.58 μm.(Courtesy F. Morier-Genoud.)*
*b) Linear SRM of the same NLFP showing a resonance at 882 nm and a FWHM of 2.8 nm (F ≈ 11).*

Spectral measurement of the back mirror after etching of the spacer shows a shift of the Bragg wavelength of 3 % towards short wavelengths. The cause was a low GaAs flux during the growth. This is the main reason of the measured low finesse. No bistability was

observed with the device, but it offered a good opportunity to measure the shift of the resonance wavelength for different incident intensities of light by nonlinear spectral reflectivity measurement (SRM) (2.2.4).

SAMPLE #360

This NLFP device sketched in Fig. 2-4 is the first one optimized for a wavelength of 885 nm. It was grown as a wedge, as sample #337, to reduce the influence of growth errors. Improvement in the calibration of the MBE-system allowed the suppression of this wedged spacer, and low thickness gradient samples could be grown.

Unfortunately, the Bragg wavelength of the rear mirror was shifted by more than 5 % towards higher wavelength because of flux problems. The sample could therefore be used only on its outer parts (where the flux was smaller during the growth). On this part, high finesse resonances (F=34) were found in the 882-890 nm range. Figure 2-7 shows a Fabry-Perot resonance with a minimum reflection of 10 % and a FWHM of 0.9 nm located at 885 nm.

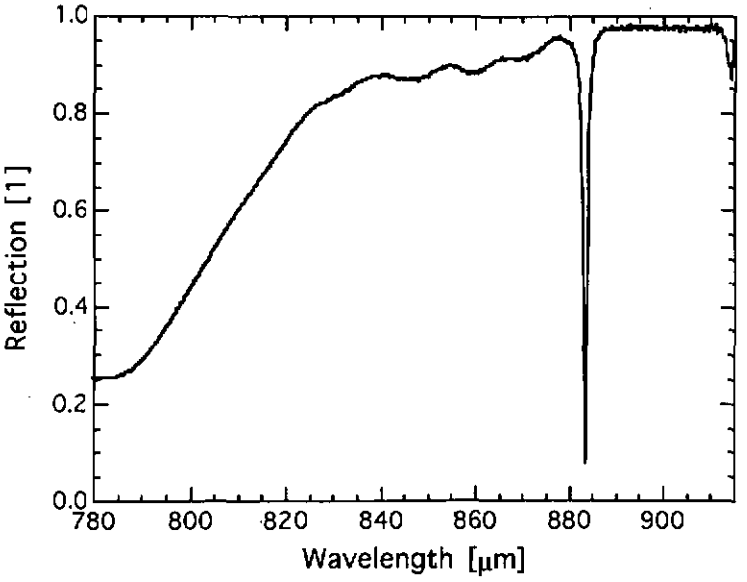


*Fig. 2-7 Reflection spectrum of sample #360 measured by linear SRM shows a high finesse resonance at 882 nm (F ≈ 34) [4].*

This sample was used for all the bistable switching measurements reported in the following section.

SAMPLE #476

The difference between this structure and the layout of Fig. 2-4 is the suppression of the GaAs monolayer included each 100 Å in the low index layers of the mirrors. These monolayers were included to enhance the interface quality and were no longer necessary with the improvements made in the growth process. The length of the low index layer was consequently modified to 744 Å.

For this NLFP, the back mirror was centered at 885 nm and with the right period. Unfortunately, the spacer was 1.9 % ± 0.1 % too short, due to a diminishing flux of GaAs of 3 % from the beginning to the end of the spacer growth. We can compare on Fig. 2-8 the resonance measured by linear SRM with the designed curve and with the simulation of the same device with a 1.9 % shorter spacer.

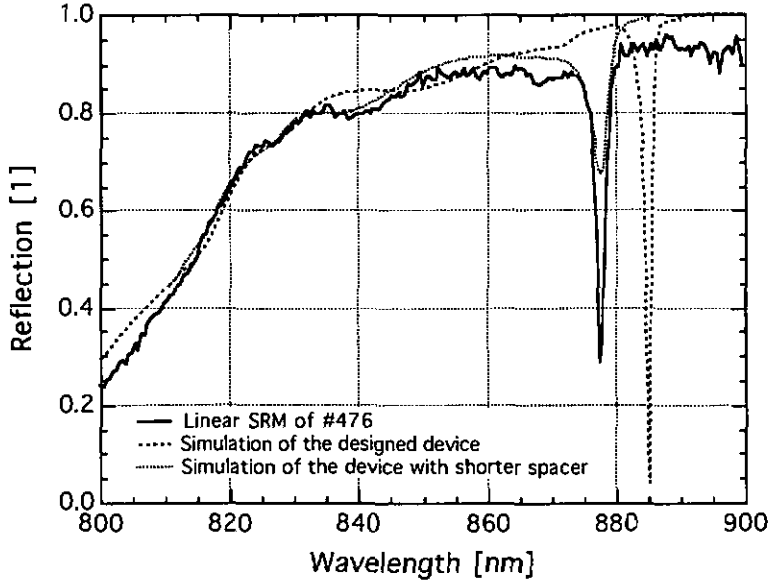


*Fig. 2-8 Linear SRM of #476 (plain line) compared with the designed curve (dashed line) and the simulation for a 1.9 % shorter spacer (dotted line).*

The NLFP is bistable at room temperature, showing a minimum threshold power of 3.3 mW at a wavelength of 875 nm with a poor contrast at switch-On (1.5:1). An impedance matched cavity is found at 879 nm. Cooled in a cryostat, it shows a minimum threshold power of 1.6 mW at 0° and 871 nm. The contrast was improved to C = 3.1:1.

SAMPLE #487

This structure, similar to the sample #476, was grown shortly after to take advantage of the MBE-calibrations for the mirrors and to correct the error in the flux of GaAs noticed during this last growth.

This sample showed again accurate periods for the mirrors but the spacer length is 1 % too long. A typical resonance at $\lambda_r$=889.5 nm, not far from the center of rotation, shows a FWHM of 0.6 nm and a minimum reflectivity at resonance of $R_{min}$=0.3.

Linear SRM spectra for different positions, parallel to the thickness gradient, are shown in Fig. 2-9. The impedance matching condition is fulfilled at a distance of about 13 mm from the rotation center at a wavelength of 882.7 nm. The wavelength change of the resonance minimum must be within ± 0.1 nm for a threshold switching power uniformity better than 10 % (Sect. 4.6). There is a distance of 125 µm along the gradient direction (vertically in Fig. 4-2), where the wavelength is constant in agreement with this tolerance at 882.7 nm (Fig. 2-9). To use the NLFP in array format it is more important to have uniformity in the threshold power than high contrast. It is therefore preferred to work near the center of the sample, where the thickness gradient is small, than at the position where the IM-condition is fulfilled. This sample was used for the measurements in array format. More about the gradient measured on that sample for the array operations of NLFPs and a complete resonance map of half the wafer is given in Sect. 4.5.1.

A threshold power of 1.4 mW with a contrast of 5.4:1 was found for $\lambda$ = 885 nm at about 13 mm from the rotation center. Near the rotation center, the threshold power is higher (1.6 mW) and the contrast lower (3.5:1). At this place, heating allowed the observation of resonances not far from the IM-condition at 60° for $\lambda$ =893 nm, but the threshold power increases to 1.8 mW.

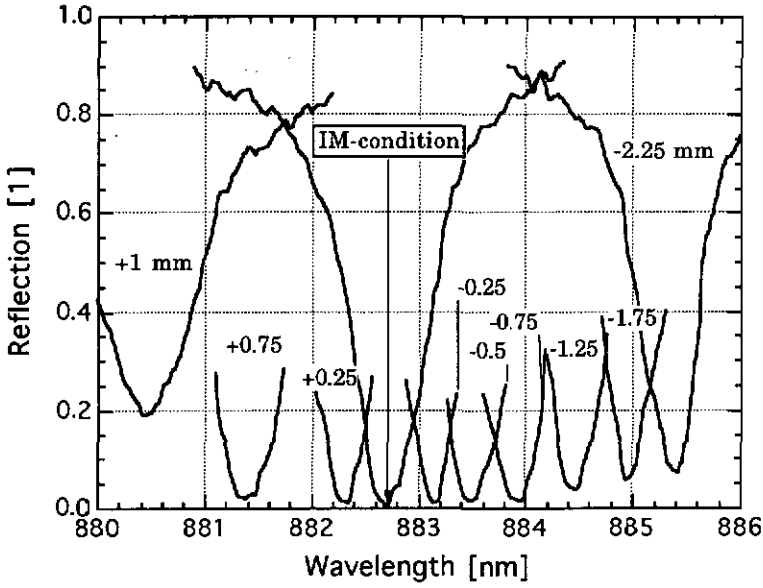


*Fig. 2-9 Linear SRM spectra of #487 parallel to the thickness gradient. The spacings from the IM-position are given in mm.*

## 2.2.3 Bistable switching of the NLFP

The first bistable switching measurements were made on sample #360. Threshold powers as low as 1 mW and switching contrasts higher than 8:1 were observed on the outer part of the wafer. The corresponding experimental results are shown in Fig. 2-10 [4].

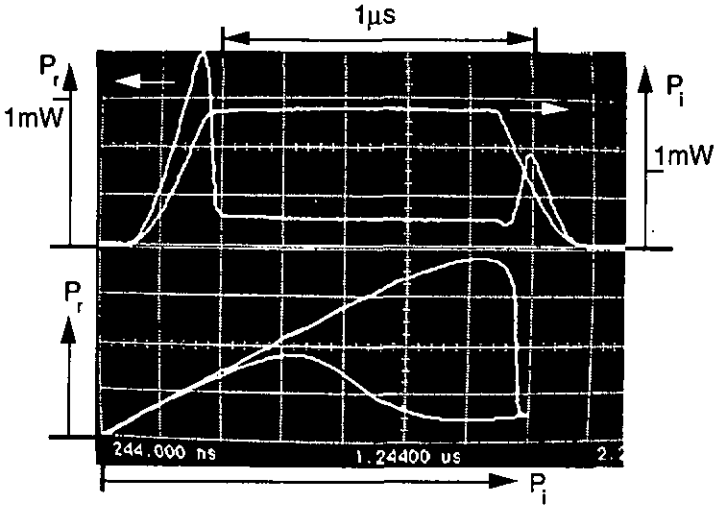


*Fig. 2-10 Bistable switching characteristics on sample #360.*
*Top : Incident and reflected power vs. time.*
*Bottom : Corresponding hysteresis plot [4].*

CRITICAL SLOWING DOWN

Critical slowing down (CSD) is a general feature of optical bistability and was first pointed out in Ref. [16]. This phenomenon describes the dependence of the switching time of the device on the excess power above threshold. In Fig. 2-11 as example, an excess power of 0 to 17 % changes the switching time from 1.3 µs to less than 100 ns. The product of transition time and excess pulse power, which can be associated with a switching energy, is approximately constant at about 15 pJ. This indicates an absorbed energy in the spacer of about 5 pJ [1].

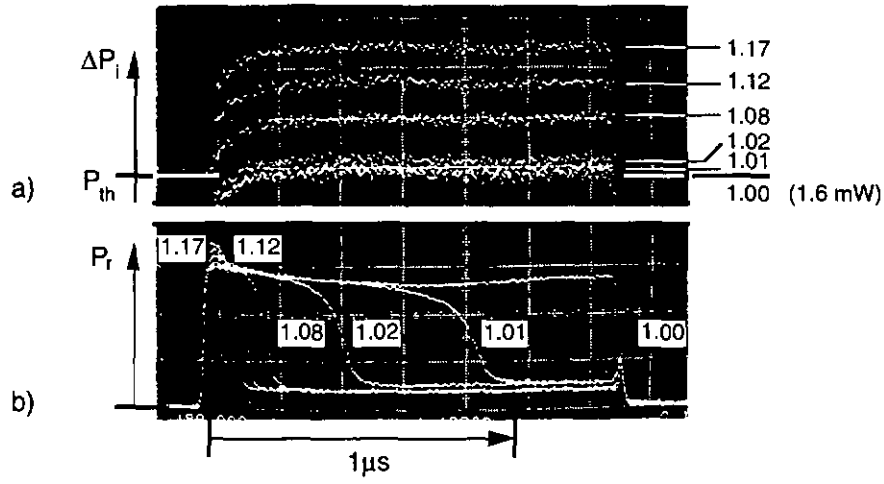


*Fig. 2-11 Dependence of the switching time on the excess power above threshold (critical slowing down).*
*a) Incident pulses which exceed the threshold of 1.6 mW by 1, 2, 8, 12, 17 %.*
*b) Reflected signal showing the corresponding switching times [17].*

THRESHOLD CRITERION

The threshold has been measured according to the critical slowing down transition between two distinct levels in the switching characteristics. This allows a reproducible measurement of the threshold power with an accuracy better than 1 % with single shot acquisition on a digital oscilloscope (cf. as example Fig. 2-11 [17]). In cases where this measurement is difficult, it is convenient to use at the same time a second method described in [18]. This method consists in defining the threshold power as the minimal power with which the horizontal tangential point in high and low reflectivity states coincides in the hysteresis plot. We found that these two methods give consistent results.

THRESHOLD AND CONTRAST DEPENDENCE ON DETUNING

The change in threshold power and contrast with the operating wavelength was also measured [4]. An almost linear increase of 1 mW/nm for the threshold power with detuning from the resonance minimum ($\lambda_r$ = 883.3 nm) was found. This threshold power dependence on wavelength detuning corresponds to the predictions of the high finesse approximation (HFA). It leads to strong requirements on the wavelength stability of the laser source (3.2.1) and on the thickness gradient of the device, if homogenous threshold power is desired over a large surface.

THRESHOLD DEPENDENCE ON SPOTSIZE

The spotsize can be varied on the sample by moving the output lens of the spatial filter (SF) in the setup shown in Fig. 2-3. Minimum threshold power was found for a spotsize of 6 μm. For larger spotsizes, the threshold power increases approximately with the spot area. For smaller ones, the power remains constant down to 2 μm and then increases. This increase can be explained by a broadening of the resonance due to diffraction losses [1].

THERMALLY STABLE SWITCHING

We measured on sample #360, without heat sinking other than through the 0.5-mm GaAs substrate, thermally stable latched switching of more than half a second [5].

## 2.2.4 Refractive index change investigation

We determine the refractive index variations for different incident powers of the laser beam (0 to 113 mW) at $\lambda$ = 882 nm. The values are deduced from nonlinear spectral reflectivity measurements (SRMs). We determine the nonlinear index change with respect to the internal intensity following a method proposed in [7]. The sample #337 is used and a spotsize of 12 μm is chosen to reduce the effects of the carrier diffusion. The SRM shows that a maximum wavelength shift of the resonance of 4.2 nm is induced by the incident power of 113 mW. A maximum negative refractive index change of 0.027 is deduced from

this wavelength shift. The internal intensity I is determined from Eq. (2-14). Figure 2-12 shows the change $\Delta n$ with respect to the cavity intensity I. The data of $\Delta n$ are fitted to a simple phenomenological two-level saturation model [19]. A saturating intensity $I_S \approx 530$ kW/cm$^2$ and a refractive index saturation value $\Delta n_S \approx 0.039$ are deduced. For low internal intensity ($I << I_S$), the material is linear with respect to the intensity and a phenomenological Kerr coefficient $n_2 = \Delta n_S/I_S \approx 7.4 \cdot 10^{-5}$ cm$^2$/kW is determined. The effect of carrier diffusion on the Kerr coefficient $n_2$ for a 12 µm spotsize is evaluated in ref. [1]. The diffusion effect reduces the value of $n_2$ by a factor of 3. The refractive index changes at wavelength below 870 nm (photon energy above gap) have also been determined and are presented in the annex A.

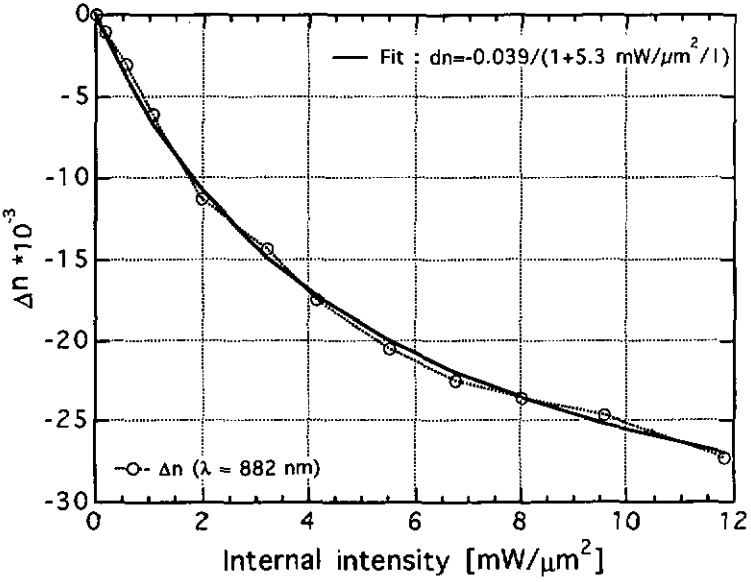


*Fig. 2-12 Nonlinear refractive index change $\Delta n$ with respect to the internal intensity I for a wavelength of 882 nm (spotsize ≈ 12 µm, sample #337). The measured curve is fitted according to a saturation model [19].*

## 2.3 Conclusion

Our NLFP is a structure made of a 2 μm nonlinear spacer sandwiched between two linear dielectric Bragg-mirrors. The spacer material, which shows highly intensity-dependent optical properties, is bulk GaAs. Multilayer AlGaAs mirrors can be integrated with the spacer in a single MBE epitaxial growth. The devices are used in reflection. They are optimized for an operating wavelength of 885 nm, with consideration of the impedance matching condition for maximum contrast. They exhibit optical bistability.

These NLFP-devices are very demanding on growth accuracy, principally considering the tolerance of 0.5 % on the spacer thickness and 1.3 % on the multilayer mirror stack period. The temperature tuning is a way of adjusting the desired absorption at the resonance wavelength when the spacer is incorrect.

Four wafers were grown according to this structure. Three of them exhibit optical bistability at room-temperature. The fourth does not exhibit optical bistability because its finesse is too low.

A setup allowing linear and nonlinear spectral reflectivity measurements (SRM) and dynamic switching measurements has been built.

Typical resonances at $\lambda$=885 nm with FWHM of 1-1.6 nm and finesses of about 35 are measured by SRM. The impedance matching condition is found at wavelengths between 882.5 and 884 nm.

Bistable switching measurements show a threshold power as low as 1 mW and a contrast of 8:1. A switching energy of 15 pJ is derived from critical slowing down measurements, corresponding to an absorbed energy in the spacer layer of about 5 pJ. A change of threshold power with wavelength detuning from resonance of 1 mW/nm is measured. The minimum threshold power is found for a spotsize of 6 μm. Tbis corresponds to a switching intensity of about 5 times higher than in the plane wave limit, which is due to diffusion effects. Thermally stable latched switching of more than half a second is obtained.

# 3 A single NLFP as element for optical computing

The physical characteristics of the NLFP as a device were discussed in Chap. 1. Here we wish to continue the discussion towards system applications. Digital optical devices can be classified by port (or terminal) where a port is either an output or an input (similarly as it is classified for electronic devices). We distinguish between two-port and three-port operation of the NLFP. In the three-port operation, the hold beam and the signal beam are separated by using different polarizations for the two beams. This external addressing using a steady state bias (hold beam) allows the isolation between the input (signal beam) and the output (reflected beam).

We study first the characteristic of the NLFP in a two-port configuration and determine the conditions for its operation in a cascadable system and the conditions for high differential gain. Second, three-port operations of the device are studied, and then we consider the advantages of transverse effects in these operations. In the third part, the off-axis addressing of the NLFP is studied in detail. Finally, the device is tested in the direction of the cascadability.

## 3.1 2-port characteristic of the NLFP

### 3.1.1 Theoretical framework

The NLFP used with one input and one output beam shows a two-port characteristic. The two-port characteristic of the reflective NLFP is shown in Fig. 3-1 a). In order to illustrate a hysteresis which is free from the influence of the lifetimes of the electron and hole carriers, the rise and fall time of the incident light pulse are adjusted to 3 μs.

Otherwise, the carrier lifetime would broaden the hysteresis loop at switch-Off (Fig. 2-10).

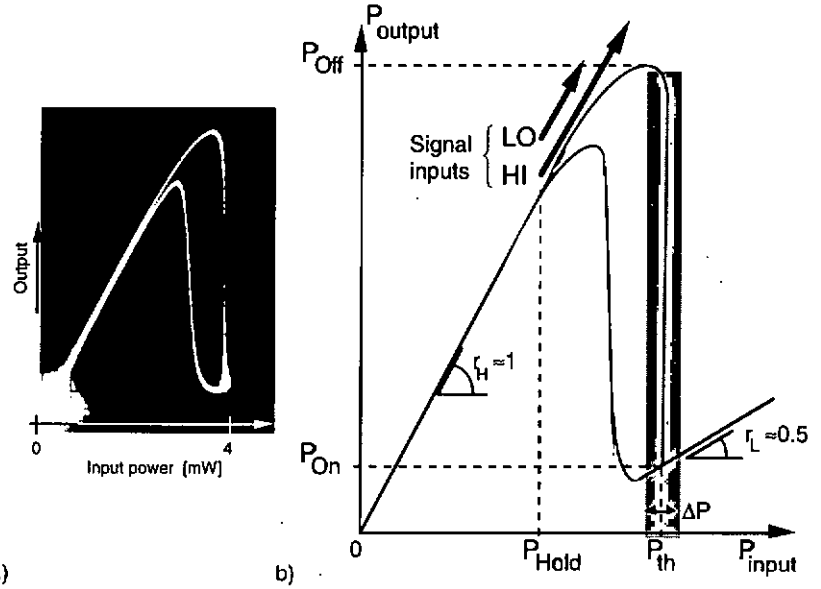


*Fig. 3-1* *a) Two-port characteristic measured on the NLFP.*
*b) Two-port characteristic of the NLFP used as a logic gate.*
*$r_H$ and $r_L$ are the differential reflectivities for the high and low reflectivity state respectively.*

Based on the two port characteristics, we can obtain differential gain by adding signal beams to a hold beam. These signals are required to implement logic functions. They must be added incoherently to avoid destructive interference. The number of signals added is called fan-in ($f_i$). The signals are either in High (HI) or Low (LO) state, representing either a zero- or a one-input. In a cascadable system, the HI state is the output power in the Off-state of the previous NLFP, attenuated by a factor (1-A), where A is the loss factor of the system, and with a factor $f_o$, which is the fan-out of the system. The fan-out is the number of signals that the output of one device can provide to the following devices. Figure 3-1 b) demonstrates the use of the two-port characteristic of the NLFP as a logic gate. The two possible output powers of the NLFP are $P_{off}$ and $P_{on}$, which are well separated if the

contrast is high. $P_{Off}$ and $P_{On}$ are given by $P_{Off} \approx R_H \cdot P_{th}$ and $P_{On} = R_L \cdot P_{th}$. $\Delta P$ is a switching window, which we define as the range of input powers within which the device might switch. Ideally equal to zero for the NLFP, $\Delta P$ is determined principally by the laser noise.

Following the equations [(3-1)-(3-2)] developed by M.E. Prise et al. [20], we can derive the relations (3-3) which describe in a convenient form the general switching conditions for the NLFP. From

$$\begin{cases} P_{Hold} + th \cdot HI + (f_i - th)LO - \dfrac{\Delta P}{2} \geq P_{th} \\ P_{Hold} + (th-1)HI + (f_i - th + 1)LO + \dfrac{\Delta P}{2} \leq P_{th} \end{cases} \tag{3-1}$$

and

$$\begin{Bmatrix} HI \\ LO \end{Bmatrix} = \frac{(1-A)}{f_o} \begin{Bmatrix} P_{Off} \\ P_{On} \end{Bmatrix} = \frac{(1-A)P_{Off}}{f_o} \begin{Bmatrix} 1 \\ (1-c) \end{Bmatrix} \tag{3-2}$$

we derive the relation

$$\begin{cases} 1 \leq f_i \approx \left[ \dfrac{P_{th} - P_{Hold}}{\Delta P} - \left( th - \dfrac{1}{2} \right) \right] \dfrac{c}{1-c} \\ 2 \leq f_o \leq \dfrac{(1-A)P_{Off}c}{\Delta P} \end{cases}, \tag{3-3}$$

where c is defined as $c = (P_{Off}-P_{On})/P_{Off}$, and the threshold th is the number of signals in the HI-state which are necessary to switch-On the device (th = 1 for a NOR-gate).

These relations show that, for a constant contrast, $f_i$ and $f_o$ are limited by the "noise" $\Delta P$. Fan-in is also limited by the threshold number th. A NOR-gate has minimum threshold. In the particular case of $f_i = f_o = 2$, Eqs. (3-1) and (3-2) were modified to Eqs. (3-1)-bis and (3-2)-bis to take into account the non-vanishing differential reflectivity that we measured in the On-state ($r_L = 0.5$). For the following calculations, we consider the worst case which can happen for the general switching conditions for the NLFP. The modified equations are

$$\begin{cases} P_{Hold} + HI_{\min} + LO_{\min} - \dfrac{\Delta P}{2} \geq P_{th} \\ P_{Hold} + 2LO_{\max} + \dfrac{\Delta P}{2} \leq P_{th} \end{cases} \qquad \text{(3-1)-bis}$$

$$\begin{cases} \begin{Bmatrix} HI_{\max} \\ LO_{\max} \end{Bmatrix} = \dfrac{(1-A)}{2} \begin{Bmatrix} P_{Hold} + 2LO_{\max} \\ P_{On} + r_L * (P_{Hold} + 2HI_{\max} - P_{th}) \end{Bmatrix} \\ \begin{Bmatrix} HI_{\min} \\ LO_{\min} \end{Bmatrix} = \dfrac{(1-A)}{2} \begin{Bmatrix} P_{Hold} + 2LO_{\min} \\ P_{On} - r_L * \dfrac{\Delta P}{2} \end{Bmatrix} \end{cases} \qquad \text{(3-2)-bis}$$

where the indices "max" and "min" means that their corresponding variables have their maximum respectively minimum values. $R_{On} = 0.25$ and $R_{Off} \approx 1$ according to experimental values. The switching window is limited to a maximum $\Delta P \leq 9.1\ \%\cdot P_{th}$ from the relations (3-1)-bis and (3-2)-bis. For this maximum $\Delta P$, we can determine the corresponding loss factor $0.485 \leq A \leq 0.515$ and hold power $76\ \%\cdot P_{th} \leq P_{hold} \leq 78\ \%\cdot P_{th}$ allowed by the system. The consequences of these relations will be used in the conclusion of Chap. 4.

## 3.1.2 Differential gain

In a cascadable system, gain (G) is necessary to compensate the losses A in the system and the fan-out $f_o$, according to the relation

$$G \geq \frac{f_o}{A}. \qquad \text{(3-4)}$$

The differential gain is defined as

$$G = \frac{P_{Off} - P_{On}}{P_{sw}} \approx \frac{P_{hold}}{P_{sw}}(R_H - R_L), \qquad \text{(3-5)}$$

where $P_{sw}$ is the power of the signal required to switch-On the device. We want to determine the favorable conditions for high differential gain G, with respect to wavelength detuning from the resonance wavelength. We choose an impedance matched device on sample 487. We use the setup described by Fig. 2-3. A special shape is given

to the input pulse using two coupled function generators to simulate the addition of the hold beam and the signal (Fig. 3-2 a)). We have the capability to independently adjust the level of both the hold and the signal beam. This allows us to determine the signal power required and consequently (Eq. (3-5)) the differential gain achievable (Fig. 3-2 b)).

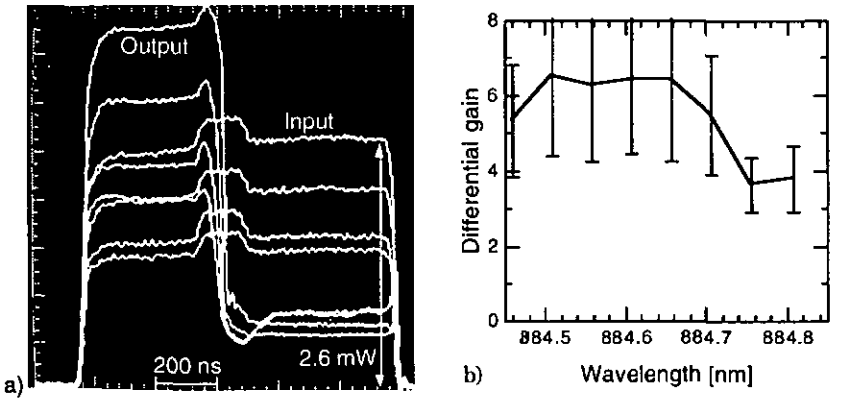


*Fig. 3-2* *a) Single input beam experiment on sample #487. Input and output pulses corresponding to different wavelengths; namely 884.66, 884.71, 884.76, 884.81 nm.*
*b) Variation of the differential gain with wavelength from the minimal threshold ($\lambda$ = 884.81 nm) to 884.46 nm.*

The power of the hold beam is set as high as possible without allowing accidental switching of the device (critical biasing). The signal power is set to induce a switch-On time (≈ 50 ns) in the critical slowing down regime. This switch-On time is approximately the same for each wavelength.

We observe that the differential gain increases from less than 4 to about 7 with increasing wavelength detuning (Fig. 3-2 b). This is a consequence of the change of reflectivity of the high reflectivity state $R_{Off}$ from 75 % to 95 % (compare to Fig. 2-5). A decrease of the differential gain for the higher wavelength detuning is explained by the increase of $R_{On}$. We can conclude that a wavelength detuning from minimal threshold power wavelength of about 1/4 of the FWHM

of the resonance is recommended in order to obtain high differential gain values up to 7.

The maximum achievable differential gain is limited to less than 10 if we wish to switch-On the device in less than 50 ns due to critical slowing down effects (Fig. 2-11). This is consistent with the limited gain-bandwidth product of 100 MHz for this structure, estimated by B. Acklin et al. [17].

The necessary critical biasing condition in the measurement, which takes its origin from working with a resonant optical cavity, is a disadvantage of this type of device compared to three terminal devices, such as the S-SEED for example. It is the main difference between bistable and thresholding devices and a consequence of the positive internal feedback of the NLFP. Because of this critical dependence, the source must have a high stability in intensity and the device must be stable in temperature. Moreover, the stability of the source with respect to wavelength is also a critical aspect for system operation. Wavelength stability better than 0.1 nm must be achieved, which is a severe requirement on the source and hard to achieve for a laser diode [1].

## 3.2 3-port characteristic of the NLFP

The NLFP used with two inputs and one output shows a three-port characteristic. The two inputs are the hold beam and the signal. They are adjusted independently and separated using the orthogonal polarizations.

### 3.2.1 Setup

The setup of Fig. 2-3 is enlarged to allow three-port operations. Fig. 3-3 describes the setup. Two orthogonally polarized beams are obtained by using the polarizing beamsplitter PBS1. The ratio of intensity between the two beams is adjusted by means of the $\lambda/2$-wave-plate. The pulses of the signal and the hold beam can be adjusted independently by means of two acousto-optic modulators. The spotsizes on the sample can be adjusted by means of a spatial

filter with a movable collimator for each beam. Spotsizes are 6 μm in order to obtain the minimum achievable threshold power of the NLFP. Oblique incidence and variable separation of the spots on the sample can be achieved by translating or rotating the mirror M1. The principal additions to the setup of Chap. 1 are listed below :

PULSE GENERATION

To modulate the second light beam, another acousto-optic modulator (AOM2) is added (IntraAction Corp., Model AOM-40N, 40 MHz acoustic carrier frequency). This modulator is used to generate the hold beam for three-port operation because the rise time of 150 ns is longer than the one of AOM1 (Chap. 1). In this case, the focusing lens before the modulator is omitted, in order to allow an efficient separation of the first diffraction order from the zero order. However, the diffracted beam has an elliptic shape ($\varepsilon = 0.6$). For shorter rise times and comparable beam shapes, this modulator is replaced by a modulator similar to AOM1.

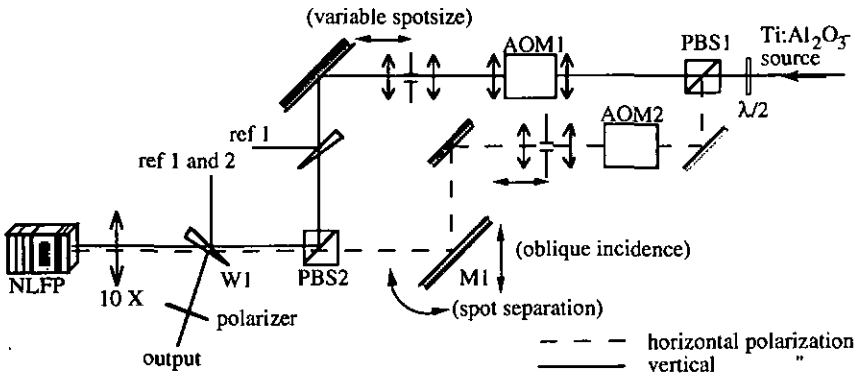


*Fig. 3-3 Experimental setup for three-port operations on the NLFP.*

OBLIQUE INCIDENCE

Oblique incidence on the NLFP is realized by translating the mirror M1 (Fig. 3-3). Coma aberrations from the microscope objective were observed for incident angles larger than 6°.

SPOT SEPARATION

To investigate crosstalk between neighboring devices (4.2) two separated spots are generated on the sample. This is achieved, as shown in Fig. 3-4, by translating and rotating the mirror M1. The distance Δs between the spots is measured on the sample by determining the distance on an enlarged image of the surface on a CCD camera. The off-axis beam is set at normal incidence by adjusting Δs and Δx.

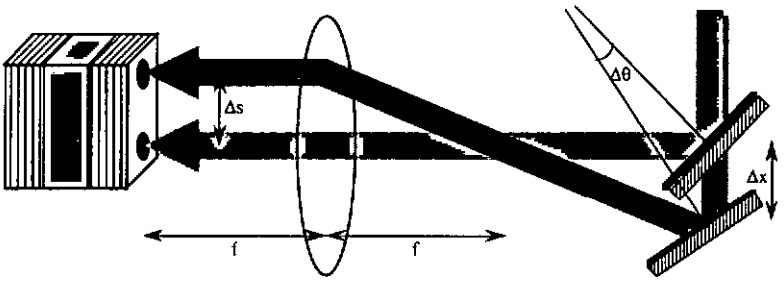


*Fig. 3-4 Generating two separated spots by translating (Δx) and rotating (Δθ) mirror M1 in Fig. 3-3.*

INCOHERENT ILLUMINATION OF THE SAMPLE AND SPACING CALIBRATION

To measure the distances between the spots and to control the wafer and the spot quality, we image and magnify the surface of the sample on a CCD camera. We use a chromium USAF 1951 resolution test target to calibrate the distances (resolution = 4 μm). The incoherent illumination of the sample is obtained by using the zero order beam of the 40 MHz AOM, which is passed through a rotating diffuser and reflected through the microscope objective by means of a glass wedge.

## 3.2.2 3-port operation

The three-port operation of the NLFP is shown in Fig. 3-5. The intensity of the hold beam of 2 μs duration is adjusted as high as possible without allowing accidental switching of the device. It lies inside the bistable region and it provides the necessary energy to bias

the device. The 200 ns signal beam is set at a power sufficient to trigger the logic operation. The output beam, which is the reflection of only the hold beam (output isolation, Fig. 3-3), demonstrates a high contrast switch-On of the NLFP in the presence of the signal beam. The curves in the top of Fig. 3-5 show a 1.4 mW power change induced by a signal pulse of 0.27 mW, i.e. a differential gain of more than 5 (Eq. (3-5)). The NLFP is shown working as an inhibiting latch, reset periodically by clocking the hold beam. The hysteresis loop in the bottom of Fig. 3-5 is obtained by plotting the measured output power versus the signal power. The hysteresis shows well defined levels for the two output states. If the change of reflectivity of the NLFP is completed before the signal beam is removed, the hysteresis is rectangular.

The three-port characteristic of the NLFP is obtained by showing the change in power of the reflected hold beam with respect to the signal input (hysteresis in Fig. 3-5). The main difference with respect to the two-port characteristic (Fig. 3-1) is the almost constant output power in Off- and On-state obtained by the elimination of the reflected signal beam and $r_H = 0$. The differential reflectivity in the On-state appears to be slightly lower than for the two-port case ($r_L \approx 0.5$).

If we consider optical logic operations, a two-port characteristic favors a NOR-gate use for the NLFP because the differential reflectivity $r_L$ in the On-state is smaller than the one in the Off-state ($r_H \approx 1$) (Fig. 3-1). For a three-port characteristic, the small differential reflectivity in the Off-state ($r_H \approx 0$) favors a NAND-gate use of the device. NOR and NAND gates form a complete logical set each, and the NLFP demonstrates flexibility of functionality.

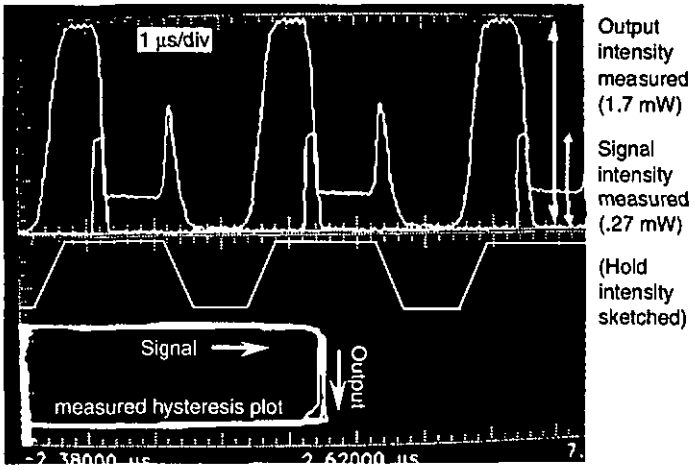


*Fig. 3-5 Demonstration of three-port clocked switching [21]. Top: Signal beam power and output beam power reflected from sample #360 vs. time. The output beam is the reflected hold beam. The incident hold beam is sketched for clarity. Bottom : Output vs. signal power (hysteresis loop).*

### 3.2.3 Transverse effects in three-port operation

For the determination of the optimum spotsize for the NLFP, the diffraction and the diffusion are taken into account (2.2.3). The importance of these effects for the NLFP is assessed in Ref. [1]. Other transverse effects influence the characteristic of the bistable switching, such as self-defocusing. At switch-On, the spacer acts as a slightly graded-index medium for the Gaussian beam, whose center creates the most negative index change. The contrast of the NLFP in reflection tends to increase [14].

We want to show that using the effect of diffusion, the information carried on a signal beam of 6 µm spotsize can be spread across the device by the use of a very large spotsize for the hold beam. In order to enlarge the hold beam spotsize by more than a factor of 10, the output lens of the spatial filter (Fig. 3-3) is displaced. We set the major axis of the elliptic spot perpendicular to the thickness gradient of the device, in order to have a constant resonance wavelength. The

signal beam is superposed on the hold beam towards the apex of the ellipse (Fig. 3-6). We take advantage of the ellipticity of the hold beam to carry the information along the major axis of the ellipse. This arrangement reduces the loss of power of the hold beam in the other direction. We can observe the surface of the sample on the CCD-camera. Without the signal beam, the NLFP is in a high reflectivity state for the whole enlarged spot of the hold beam (with about 90 μm of extension in the largest direction). With the signal beam, the NLFP is switched over a central area of 60 μm x 20 μm.


*Fig. 3-6 The critically biased NLFP on sample #360 is switched-On over a distance of 60 μm by a 6 μm spotsize signal beam. The dark ellipse at the center of the large spot is the zone where the NLFP is switched-On.*

We observe the NLFP switch-On as a complete entity in two cases. First, when the hold beam is more extended than in normal conditions. Second, when the signal beam is of much smaller spotsize than the hold beam. These results can be explained by the theory of switching waves in the transverse direction of the bistable device [22]. Calculations developed by Sfez [23] allow us to estimate that the switch-On time of the whole enlarged device is slow (in the order of microseconds). It is also concluded that the switching waves reduce the width of the observed hysteresis loop by a factor of two compared to a plane wave model at switch-Off.

## 3.3 Off-axis address of the NLFP

The principle of off-axis address is illustrated in Fig. 3-7. The oblique incidence of the signal beam on the NLFP will cause a reduction of the effective thickness of the device from L to Lcosθ (θ is the angle inside the device, related to the external angle of incidence $\theta_i$ by Snell's law). A change in resonance wavelength $\Delta\lambda_{res}$ is induced, which scales quadratically with the incident angle [1]. Consequently, the hold beam, which is incident normally, ensures the critical biasing at the low wavelength side of the resonance and the signal beam, which is incident obliquely, triggers the switching efficiently at the wavelength of the resonance, because the resonance is shifted.

In order to estimate a useful angle θ, we start with the angular acceptance of the basic device cavity.

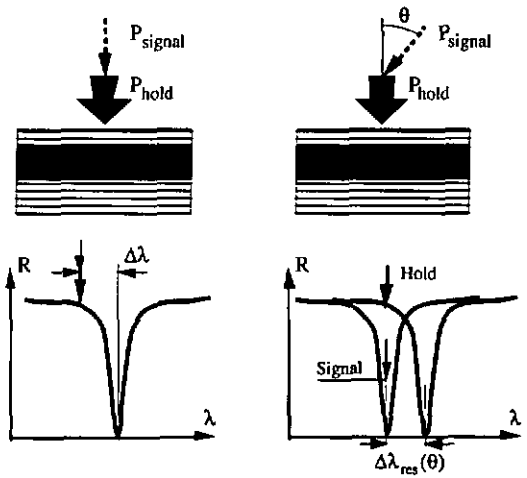


*Fig. 3-7* *Illustration of the principle of the off-axis addressing. Left : The signal beam is incident normally, parallel to the hold beam. Both beams are spectrally detuned from the same resonance minimum. Right : The signal beam is incident obliquely, and is efficiently absorbed because the resonance wavelength is shifted for the signal beam towards lower wavelength.*

From mathematical relations developed in Ref. [1], we estimate this angle of acceptance of the NLFP to be limited to 11° due to diffraction. The limitation in angle will reduce the spatial fan-in capability of the NLFP. This spatial fan-in capability is evaluated to be two for the basic structure [1]. An off-axis arrangement for the signal beams is the way to utilize the spatial fan-in capacity of the NLFP. We consider two coherent signal beams separed with an angle of 20°. They will form interference fringes with a spacing between the fringes of 2.5 μm. The consequences of the interference effect will be averaged over the 6 μm spotsize and washed out by diffusion.

### 3.3.1 Gain improvement

Jin et al. [24] showed theoretically that the differential gain in GaAs bistable etalons can be enhanced by a factor of two with an incidence angle of 18° for the switching beam. We understand this improvement in the differential gain by a better coupling on resonance of the signal beam. A signal beam of $9/22 \cdot P_{sw}$ of power coupled ideally on resonance would have theoretically the same effect as a signal of $P_{sw}$ in normal conditions [1]. To couple better the signal beam into resonance without a change in wavelength with respect to the hold beam, it must be set with an oblique incidence.

We want to verify experimentally the enhancement of the differential gain with a nonzero angle of incidence of the signal beam. By translating the mirror M1 (Fig. 3-3), the oblique incidence of the signal beam can be achieved. The hold beam remains on-axis. The duration of the hold and the signal pulses is set to 2.8 μs and 100 ns respectively. We measure first the threshold power for the NLFP illuminated with one beam, and then the power for switching it ON using the hold and the off-axis signal beam added together (for angles between 0° and 11°) (Fig. 3-8 left). To reduce the influence of the noise of the laser, each measurement is averaged over 32 pulses. All measured powers are determined for a constant switching time. The error in the measurements of the signal power is estimated at 17 % due to the fluctuations of the power of the hold beam. A power of 0.15 mW in excess to the threshold power is necessary to switch-On the NLFP using the 100 ns signal, because an energy of 15 pJ is required (2.2.3, CSD-effect). Therefore we express the observed

changes of the power required for the switching in the measurements of Fig. 3-8 left by the changes in excess power vs. angle in Fig. 3-8 right.

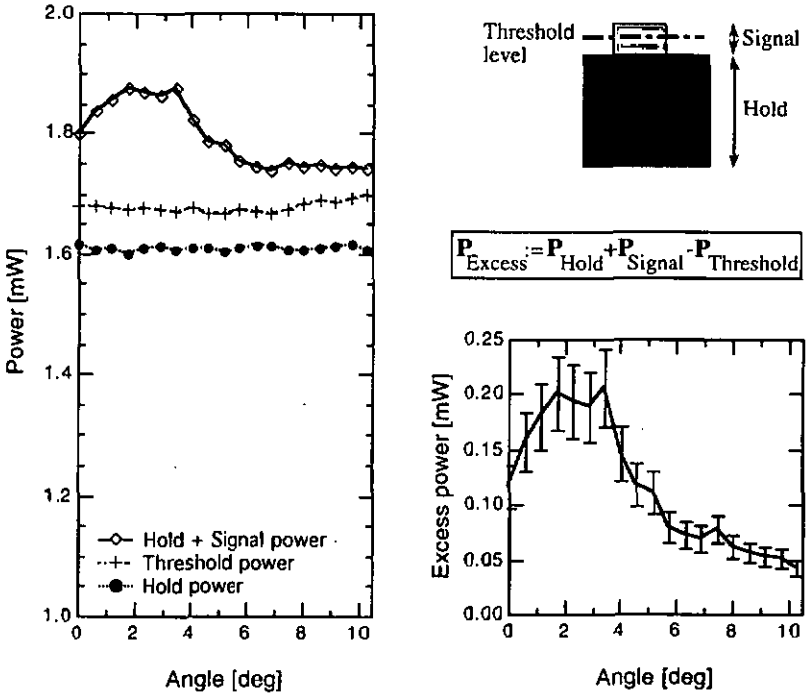


*Fig. 3-8 Power of the hold and the signal beams compared to the threshold power (left), and power of the signal beam in excess of the threshold power, which is necessary to switch-On the NLFP (right).*

We observe a tendency of the excess power to decrease as the angle increases. This tendency seems in agreement with the presented theory. The initial increase of the excess power for small angles can be explained by a diminishing overlap between the spots. The decrease of the excess power, predict by the theory, is quadratic as a function of the angle, and therefore negligible for small angles. Since the noise in the hold beam power induces a large error in the measurements of the signal power, we are unable to verify the predicted improvement of the differential gain. We can conclude that

an off-axis addressing of the signal beams on the NLFP is favorable because it allows spatial fan-in and it seems to improve the achievable differential gain for angles between 6° and 10°.

SETUP PROPOSITION

The setup proposed in Fig. 3-9 seems conceivable for three-port operations on an array of NLFP. It allows a hold beam incidence on-axis and a signal beam incidence with an angle of 10°. The signal beam is in this case the reflection of the hold beam on a blazed grating. With this imaging system, using two lenses, the waist of the output beams on the grating are "imaged" onto the NLFP. The signal beams could also be provided by a surface emitting laser (SEL) array placed vertically at the place of the blazed grating. A wedged plate should be placed in front of the SEL array to allow the precise positioning of the waist of each signal beam exactly on the surface of the NLFP.

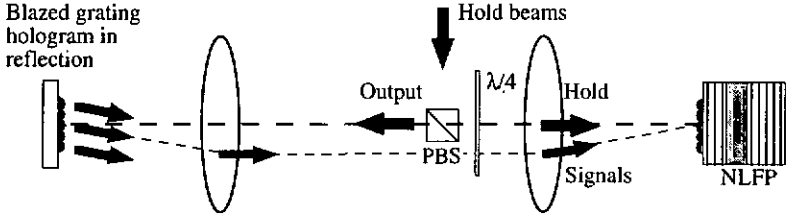


*Fig. 3-9 Off-axis arrangement for the imaging of a reflected array of hold beams as 10° incident signal beams on the NLFP.*

### 3.3.2 Hold beam off-axis

From a system point of view, it can be desirable to have the non-normal incidence of the hold beam on the NLFP. It is clear that in this case the increase of the losses mainly due to beam walk-off will lead to a loss of finesse. A decrease in finesse induces an increase of the threshold power (Eq. (2-16)). We assess here the changes in finesse, contrast and threshold power which can be induced by an off-axis incident beam on the NLFP.

An oblique incidence of the beam can be obtained by translating the mirror M1 in the setup of Fig. 3-3. We measure the changes in the resonance of the NLFP for a normal and an off-axis incidence of the beam. In Fig. 3-10, the loss of finesse of the resonance vs. angle is shown by plotting two spectral reflectivity measurements (SRM) with 3 mW of incident beam power, the first with normal incidence and the second with an incidence angle of 5.7°. A third SRM at 5 mW is added, also with an incidence angle of 5.7°. From the two SRM at 3 mW incident power, we can determine that the optical bistability is lost with the angular incidence. A bistable switching in a SRM is determined by a jump from high to low reflectivity with a small wavelength change (an infinite spectral differential reflectivity). The on-axis curve shows a bistable change at $\lambda = 887.2$ nm. The second curve at 3 mW with 5.7° of angle of incidence shows no bistable change, but an increase in FWHM from 1.13 nm (on-axis incidence) to 1.75 nm. It is necessary to increase the incident power to 5 mW to observe the bistability again. The measured wavelength change of -0.23 nm for 5.7° is in agreement with the simulations (2.1.2), which predict a change with angle of -0.19 nm for 5° (and -1 nm for 12°). This is lower than the value of -0.26 nm for 5° obtained from a simple estimation [1], which shows that the wavelength change behaves quadratically with respect to angular change.

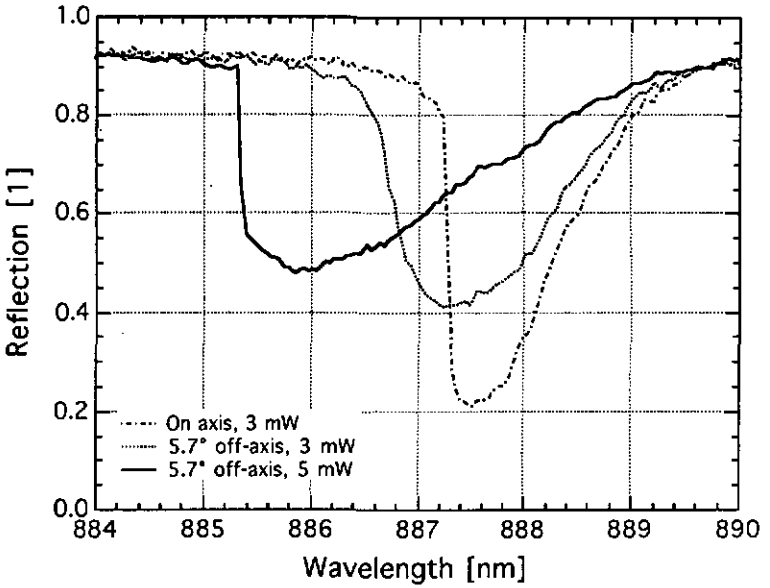


*Fig. 3-10 Reflectivity vs. wavelength for two different angles (0 and 5.7°) on the sample #360. The input powers are 3 mW on-axis, and 3 and 5 mW off-axis at 5.7°.*

The change in the threshold power and in the contrast at switch-On with respect to the change of angle can be determined by dynamic switching measurements. The measurement of this change is reported in Fig. 3-11. We observe an almost linear decrease of the contrast which is a consequence of the loss in finesse of the NLFP. We determine also a quadratic increase of the threshold power which is the consequence of the same loss of finesse.

Consequently, off-axis incidence of the signal beam should be avoided for angles larger than 1°, because the contrast of the switching decrease by about -0.89 between 1° and 4°. The threshold power is robust against small angle variations because it depends quadratically on the angle, but it increases rapidly for angles larger than 2°.

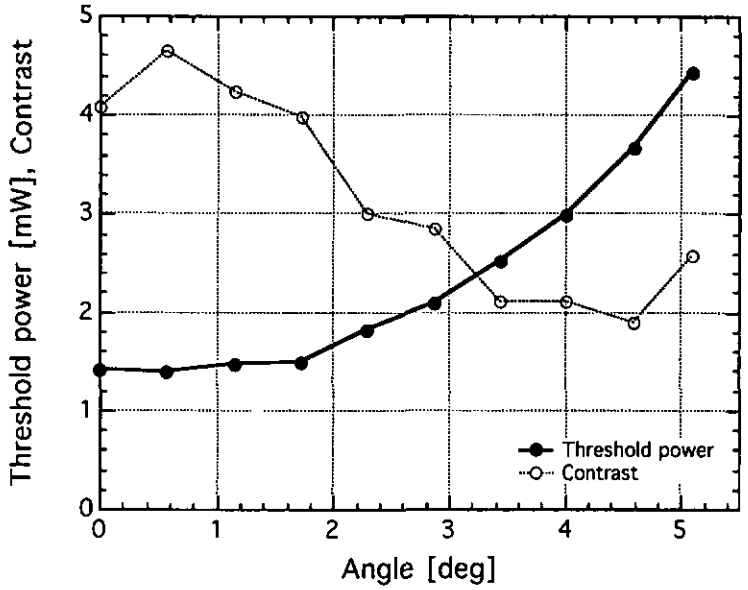


*Fig. 3-11 Change of minimum threshold power and of contrast for different angles of incidence of the input beam on sample #360 ($\lambda$ = 885 nm).*

## 3.4 Demonstration of the cascadability of the NLFP

A device is cascadable if its output is able to trigger at least one succeeding device. Cascadability is a requirement for devices which are inserted in more complex systems [25]. The aim of this section is to demonstrate that the NLFP acting as a bistable gate can drive another similar gate with its output. Here, the second gate is the same NLFP. The capacity of the device to drive more than one gate (fan-out capability) will depend on the achievable gain or on the operation cycle (3.1.2). The latching capability of the NLFP is not used here, since the signal beam has exactly the same duration as the output beam.

### 3.4.1 Free-space delay line (24 ns)

The lifetime of the carriers in the NLFP is of the order of 4 to 10 ns. A delay line of more than 10 ns is therefore necessary to use the output of one NLFP as a signal for itself. We obtain a 24 ns delay line by constructing a 4-f system with lenses of 1 m focal length. The output beam is reflected after 4 m on a mirror to be redirected on the sample as an on-axis signal beam (Fig. 3-12). The signal beam shows a normal incidence on the sample for setup convenience, as the fan-in is 1 for this experiment. The total distance covered by the beam is about 8 m leading to the measured delay of 24 ns.

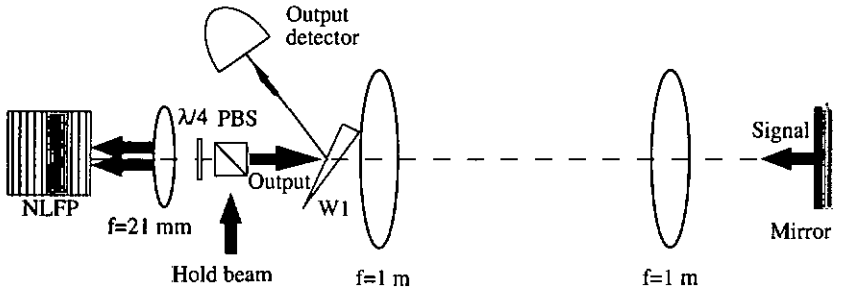


*Fig. 3-12 Setup used for taking advantage of the output beam as an on-axis signal beam delayed by 24 ns.*

To demonstrate the cascadability of the NLFP, it is demanded that a high reflection output (Off-state) will switch-On the following NLFP and a low reflection output (On) will not switch-On the next one. This is not possible using this delay line. The main reason is that the NLFP is determined by a switching energy requirement (Chap. 1) which implies a limited gain bandwidth product (GBWP) which is essentially equal to the carrier relaxation rate $\tau^{-1}$ or 100 MHz [1]. Therefore, the cycle of operation of about 40 MHz imposed by the delay line allows only a low differential gain. This differential gain will at maximum compensate the losses induced by the large number of glass-air interfaces, which are necessary for the delay line of Fig. 3-12. To demonstrate cascadability, a larger differential gain is necessary and consequently, if the losses in the setup cannot be reduced, the frequency of operation of the NLFP must be decreased.

However, 7 MHz operation of the NLFP with gain can be demonstrated. The results are shown in Fig. 3-13 with the use of the setup of Fig. 3-12. Only the output beam is shown on the Fig. 3-13. The bright trace represents the reflection of the hold beam when no signal beam is present, and the faint trace represents the reflection when hold and signal are combined on the sample. The traces are inverted (negative-values), because a faster detector which shows a negative output had to be used for this experiment (Model HP81519A, DC-400 MHz, light input by use of a multimode fiber). The hysteresis plot (bottom) is obtained from these two traces, the switched-On output vs. the output if no signal is added. As the bright trace is the linear reflection of the input beam, the hysteresis can be compared with the usual hysteresis of bistability (Fig. 2-10).

The critical slowing down transition (rising edge of faint trace) takes 40 ns. From this we can determine that with the setup used, the device will limit the operation frequency to about 24 MHz. This seems consistent with the estimated GBWP of 100 MHz, taking in consideration the losses in the setup.

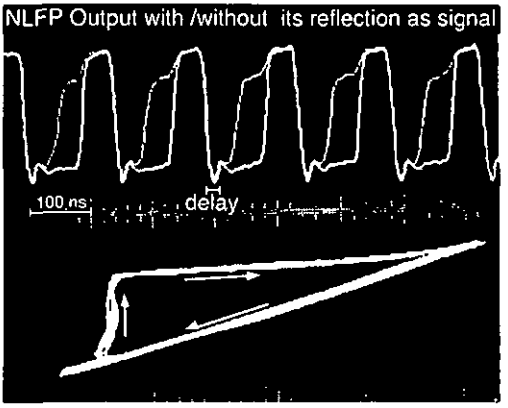


*Fig 3-13 : Top : The bright trace is the reflected power of the NLFP #487 without signal beam . The faint trace is the reflected power with a signal beam which is the 24 ns delayed reflection of the output.*
*Bottom: Corresponding hysteresis plot.*

### 3.4.2 Delay line using a monomode fiber (260 ns)

We concluded in Sect. 3.4.1 that the cycle of operation of the NLFP, which is set by the delay line, must be low enough to allow high gain according to the GBWP of the device and consequently cascadable operation. We construct a ten times longer delay line in order to increase the available gain. The long distance required favors the use of a monomode fiber. The output beam of the NLFP is injected after the wedge W1 (Fig. 3-12) into a 25 m monomode fiber by means of a 10X microscope objective. A gold mirror of 98 % reflectivity is glued at the other end of the fiber. The total delay of the line is 260 ns. Dispersion is not observed in the fiber, and the losses are essentially injection losses.

The reflected output beam will be used as an on-axis signal beam in the three-port setup (as before). A LO output state will induce an On-state in the next operation and a HI output state an Off-state and so on. The pulsing behavior is demonstrated in Fig.3-14. The hold beam (top) shows a pulse each 260 ns. The shape of the pulse has to be modified to observe the pulsing effect. A large excess of power is necessary to allow a fast switching of the NLFP according to the Fig. 2-11 (critical slowing down (CSD) effect). We need this excess of power only at the beginning of the pulse, to trigger the switching. It must be removed shortly after, because otherwise it will induce the switching with the low signal beam alone (15 pJ of switching energy requirement for the NLFP 2.2.3, CSD). The second trace (bottom of Fig. 3-14) displays the output beam, revealing a switched-on NLFP every second pulse of the cycle, because the reflected output beam is a signal in HI-state each two pulses. A pulsing behavior with few errors (bit error rate (BER) of about 0.05) is obtained.

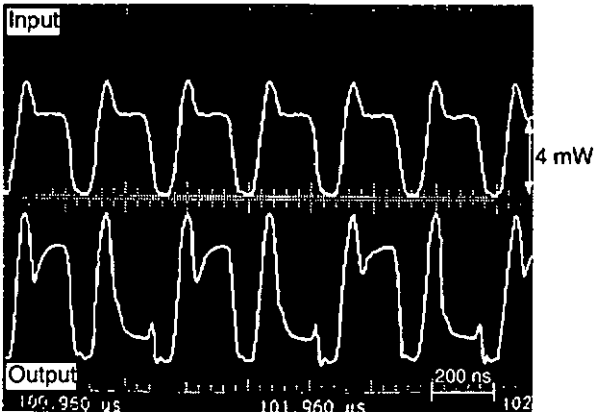


*Fig. 3-14 Top : Power of the hold beam pulse vs. time. A pulse is send each 260 ns (duration of the delay of the line).*
*Bottom : Power of the output beam vs. time, demonstrating the switched-On NLFP #487 every second pulse.*

## 3.5 Conclusion

The device demonstrates two-port operation with differential gain up to 7. The favorable spectral detuning for high differential gain is determined to be about 1/4 of the FWHM of the resonance from the minimum threshold wavelength. The differential gain is limited to 10. The device shows the critical biasing requirement which is disadvantageous because the device can amplify the noise of the source. As other consequences of this requirement, the NLFP must be stable in temperature and the source must show a wavelength stability better than 0.1 nm.

The setup of Chap. 1 is enlarged to allow three-port operation of the NLFP and operations using an input beam with angular incidence. Three-port operations are demonstrated on the NLFP at high duty-cycle, showing this device acting as an inhibiting latch. Differential gain of more than 5 is shown in this configuration.

Transverse effects can increase the switching-time of the NLFP and increase its spatial fan-in capabilities. The device shows a switch-On

as a complete entity when it is extended to several tens of micrometers and when the signal beam is much shorter than the hold. This is a consequence of the switching waves phenomenon.

Theory predicts an improvement in the differential gain up to a factor of two if the signal beams are fanned-in off-axis. This off-axis addressing of the signal beam is tested, essentially because it is the way to profit from the spatial fan-in capability of the NLFP. We measure a tendency for the signal beam power required for switching to decrease using a constant hold beam power and an increasing angle. This tendency to increase the differential gain leads us to conclude that it is advantageous to input the signal beams at angles as high as 10°. Consequently, it is preferable to address the NLFP with two independent off-axis signal beams. The hold beam should remain on-axis ±1° to avoid a loss of finesse and an increase of the threshold power of the device.

The NLFP is a cascadable device. It is possible to get cascadable operations at 4 MHz using a delay line of 260 ns effected by the use of a fiber with a mirror glued at one end. However, it is not possible to get cascadable operations at 40 MHz (delay line of 24 ns) because of the limited gain bandwidth product of about 100 MHz and the losses of the delay line.

# 4 Operations in array format

## 4.1 Introduction

An advanced system architecture using all-optical switching devices may exploit the full parallelism inherent in the optics system using space invariant interconnection holograms for the optical wiring [26]. Some device constraints on the architecture were outlined in the preceding chapter. An on-axis incidence of the hold beam is required and an off-axis incidence of the signal beam is favorable. It is also important to operate in reflection. These system architecture constraints seems to favor the use of free-space optical wiring between the devices. The next step towards the implementation of the NLFP in an advanced system is therefore to study its behavior as a device in array format.

To this aim, first, we want to determine precisely the minimum spacing between the devices in the array. Second, we relate the characteristics of the sample #487 which are important for simultaneous operation of many devices on an area of its surface. Third, we show the method of spot generation for a small array of spots and describe the complete setup. Forth, we study the switching characteristics of the NLFP in array format using two methods for detection.

## 4.2 Crosstalk between coupled devices

In array operation, the position of each device will be determined by the spots created by the incident beams (optical pixellation). The spacing between each NLFP must be determined accurately to allow only a negligible crosstalk between the devices, which will leave their individual characteristics unchanged. This may not be the case for

other pixellation techniques such as reactive ion etching [27] or defect-induced alloy-mixing [28]. We want to determine the separation between the devices for low crosstalk.

The setup used for three-port operation (Fig. 3-3) allows the adjustment of the spacing $\Delta s$ between two beams incident normally (Fig. 3-4). The two beams are incident simultaneously on the sample, each one with a spotsize of 6 μm, and their corresponding NLFPs show similar threshold power (±3 %). One beam is moved (beam 2) along the low thickness gradient direction of the wafer and remains at constant power. A decrease in the threshold power for the beam 1 is observed when the distance $\Delta s$ between the two spots is reduced. This decrease in threshold power is due to the carriers generated in the region illuminated by the beam 2 which diffuse through the sample to the spot 1. The detailed measurements are reported in Fig. 4-1. The figure shows the change in threshold power for the beam 1 as a function of $\Delta s$. For each spacing $\Delta s$, the threshold is measured with and without the presence of the beam 2. The beam 2 is set at the threshold power for the first series of measurements (plain line) and at half this power for the second one (dashed line) [21].

The measurements of Fig. 4-1 show the clear influence of a diffusion coupling at spot separations up to 50 μm for two similar spots at threshold power. This is more pessimistic than earlier results by Jewell et al. [29], which showed that the crosstalk begins to be noticeable at about half this separation and also more than the theoretical results of Firth et al. [30] which predicts a separation of a few diffusion lengths for a noticeable crosstalk in 1-dimensional arrays. However, we find a coupling influence of only 1.8 % when the separation between the two devices is $\Delta s = 25$ μm and one of the devices is at threshold. In a 2-dimensional array, we can assume that the total influence of neighboring devices is about 5 times higher than the crosstalk from a single device. We estimate that a separation of 50 μm between the devices of the array is a good choice to avoid the influence of crosstalk. A tolerance of 5 % in the threshold power must be ensured using this separation.

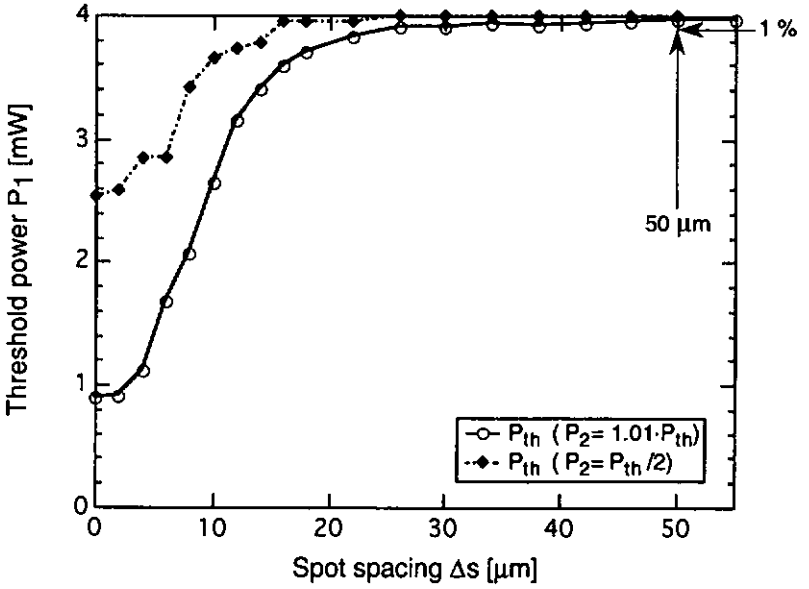


*Fig. 4-1 : Variation of threshold power for a spot in the presence of a second spot as a function of the spacing Δs between the two spots. The second spot is unswitched (dashed line) and switched (plain line) [21].*

## 4.3 Study of the sample #487 towards operations in array format

We decided to use the sample #487 for the operation of the NLFP in array format because it shows a large area where the thickness gradient is small and the resonance wavelength is constant (2.2.2). Here we report the resonance contours of this sample and the results of single spot switching at selected spots throughout this area.

## 4.3.1 Characteristics of the wafer #487

LINEAR CHARACTERISTICS

In order to determine the resonance contours of the sample #487, we image its surface onto a CCD-camera and illuminate it with the laser beam. The resonance contour at the laser wavelength appears as a dark fringe on the illuminated zone. On changing the laser wavelength we can add the contours at different wavelengths to obtain the Fig. 4-2. The figure shows these contours at different wavelengths on the half of the sample #487B which will be used for the next measurements. The dark fringes of the resonances show concentric circles because the sample was grown with rotation.

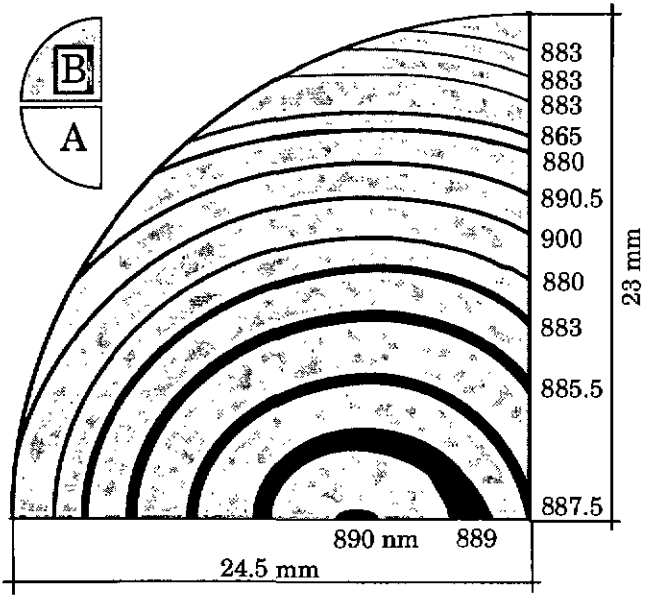


*Fig. 4-2 Resonance contours on the sample # 487B.*

The figure shows resonance wavelengths from 890 to 865 nm. We determined that a resonance at 885 nm corresponds to the same dark fringe as a resonance at 915 nm, leading to a free spectral range (FSR) of about 30 nm. This is in agreement with the FSR of 36 nm

calculated from theory (Eq. (2-11)) which takes into account the dispersion of the refractive index. This is also in agreement with the FSR of 33 nm measured by spectral reflectivity measurement (Annex). A typical FWHM of the resonance at 885 nm is equal to 0.7 nm (Fig. 2-9) from which we calculate a finesse of 50 and an absorption of $\alpha \approx 160\ cm^{-1}$ (Eq. (2-13)).

We can estimate the thickness gradient of the device from the change in resonance wavelength [1]. The resonances contours are shown in Fig. 4-2. The change in resonance wavelength is less than 1.5 nm for a 10 mm diameter disk at the center of the sample, showing less than 0.3 % of thickness change. A change of wavelength of 5 nm (from $\lambda$=889.5 nm to 884.4 nm) is determined on a 10 mm line parallel to the gradient, leading to a thickness change of less than 0.1 % pro mm.

DYNAMIC CHARACTERISTICS

The appropriate place for operation in array format is at the low gradient position near the center of the specimen. At this place we measure a typical threshold power for bistability of 1.6 mW and a contrast ratio between 3 and 4:1 at $\lambda$ = 888.7 nm. The contrast is low because the NLFP does not fulfill the impedance matching condition (IM for $\lambda$ = 882.7 nm). The two-port switching characteristic is reported in Fig. 4-3 a). A short duration signal beam of 0.3 mW power is added to the hold beam of 1.6 mW (first trace, top). The output beam shows that the NLFP switches-on during the presence of the signal beam (second trace, top). The corresponding hysteresis plot is shown at the bottom. The butterfly shape of the plot is due to the short rise time of the pulse (25 ns) and a small electrical delay in the cables for the reference and the signal detectors. In Fig. 4-3 b), four 3-D plots describe the switching of the NLFP as detected on the CCD-camera where the device is imaged. The plots correspond to increasing power from left to right of: below threshold, at threshold ($P_{th}$ = 2 mW), above threshold ($1.02 \cdot P_{th}$ and $1.2 \cdot P_{th}$). We observe a change in reflectivity of the device due to switching between the second ($P_{th}$) and the third ($1.02 \cdot P_{th}$) plot.

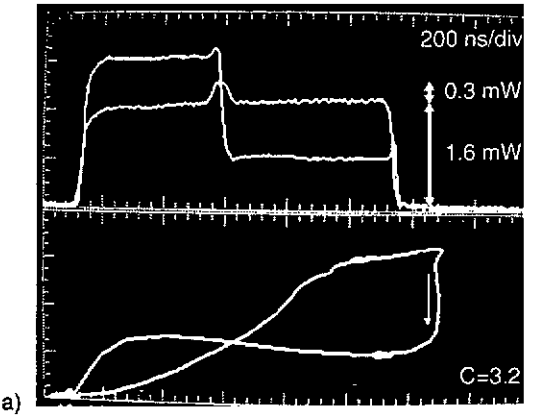


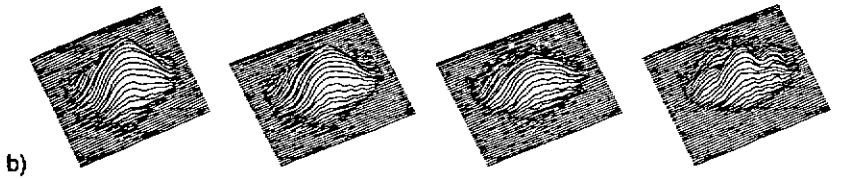


*Fig. 4-3* *Switching characteristic near the center of the sample #487 at $\lambda$=888.7 nm.*
*a) Top : input and output power vs. time. The input power consists of a 1 µs hold beam with a 80 ns signal beam added;*
*Bottom : Corresponding hysteresis plot.*
*b) 3-D plots of the switching detected with a CCD-camera, at powers below threshold, at threshold ($P_{th}$ = 2 mW), just above (1.02·$P_{th}$) and above threshold (1.2·$P_{th}$).*

## 4.3.2 Single beam investigation of 3x5 NLFPs

We wish to determine the threshold power which is needed for the bistable switching of each element of the array using a single beam investigation. The conditions of the measurement (place and wavelength) are exactly the same as will be used in the further measurements in array format. The sample is moved by 50 µm between each two-port single measurement of the threshold power. The threshold power is determined following the method described in

Sect. 2.2.3. The measured threshold powers are reproduced in Fig. 4-4.

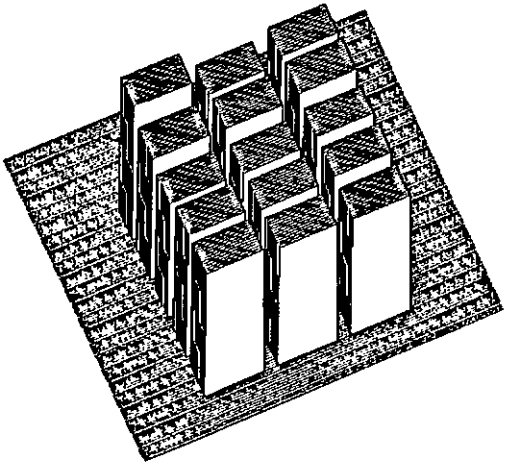

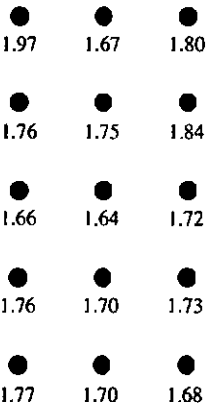


*Fig. 4-4 Measured threshold powers at the positions where the fan-out will produce the spots of the array. The results are represented as a 3-D plot with the power values in the z-axis direction (left) or as the measured threshold powers at each location (right).*

We measure a mean threshold power of 1.74 mW. A standard deviation of 4.6 % of this mean is found for the 15 measured powers. These measurements are reproducible. For repositioning in the x- and y-directions we use a step-motor with 2.5 μm steps. We estimate an accuracy in displacement of about 2 μm.

The significant change in threshold power measured at different places is surprising in reason of the measured low thickness gradient of Fig. 4-2. We further measured finely the threshold powers in-between the three data points ($P_{th}$ = 1.64, 1.75 and 1.67 mW in Fig. 4-4). We move the sample by 7.5 μm steps. The measured threshold powers are plotted with respect to the separation distance from the center of the array in Fig. 4-5. For the original data points we now find threshold powers of $P_{th}$=1.66, 1.78, 1.7 mW, respectively. The measured change of 1.8 % in the three data points is explained by the threshold measurement accuracy of ± 1 % and the accuracy in

displacement. A maximum change of 10 % in the threshold power is found over the measured distance of 100 µm. We observe in Fig. 4-5 that important changes in the threshold power can occur for small variations of the distance (maximum 6.8 µW-change pro micrometer). We have no definitive explanation for these changes. Consequently, the repositioning must be ensured better than 5 µm to allow reproducible threshold measurements on sample #487.

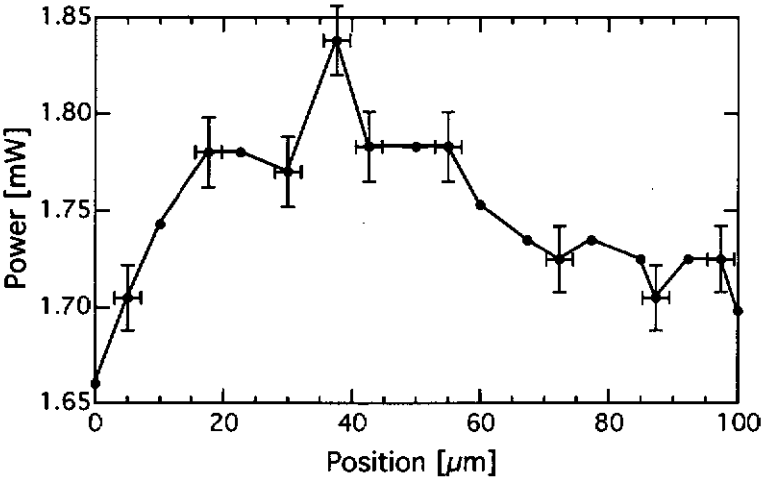


*Fig. 4-5 Threshold power measured at λ = 888.7 nm over the distance from the center point (1.64 mW) of the future array to the top (1.67 mW) of the column at the center (Fig. 4-4).*

## 4.4 Setup for array operation

The array of beams is generated with a Dammann grating or a continuous surface relief fan-out element, which are both designed at our institute. The last element is dimensioned for low wavelength sensitivity and shows a slight better efficiency (82 %) than the Dammann grating. Nevertheless, we use the Dammann grating for the following measurements, because it shows a better uniformity at 890 nm. We generate 3x5 beams. The number of beams in the array

was limited according to the available optical power delivered from the 600 mW Ti:$Al_2O_3$ laser.

### 4.4.1 Spot generation

The Dammann grating was designed to generate diffraction orders of equal intensity at 885 nm. It was designed and fabricated at IMT. The hologram is fabricated on a glass substrate using photolithography and ion beam milling.

The period of the fan-out element is 380 µm, to generate 50 µm spaced spots on the bistable element using a Fourier lens of f = 21.5 mm focal length. We verified experimentally the spacing between the spots on the sample to be 50 µm ± 1 µm and also the 6 µm spotsizes which are generated by illuminating more than 110 periods of the fan-out element. The large number of illuminated periods diminishes the influence of local defects.

A uniformity of 10 % is measured at 890 nm. The uniformity is defined as $(I_{max}-I_{min})/(I_{max}+I_{min})$. The non-uniformity of the CCD-camera allows only ± 4% accuracy in the measurement of intensity (4.4.3). This induces an absolute error of ± 6 % in the measurement of the fan-out uniformity. The measured efficiency is 80 % at 890 nm. No fine angle adjustment of the fan-out element is necessary, because the uniformity of the element is only slightly dependent on the incident angle of the beam. The uniformity changes from 10 % to 9.95 % for an angle of ± 2.4°.

### 4.4.2 Experimental setup

The setup used for the following measurements is described in Fig. 4-6. The spatial filter is set to reshape the hold beam in order to obtain a 4 mm diameter waist on the fan-out element. The 5 x 5 mm polarizing beamsplitter (PBS2) reflects the 3x5 perpendicularly polarized beams generated by the fan-out element to the sample and allows the separation of the output from the hold beam when a λ/4-wave-plate is inserted between the PBS2 and the sample. The 3x5 beams are focused on the sample by a high quality Fourier lens of 21.5 mm focal length.

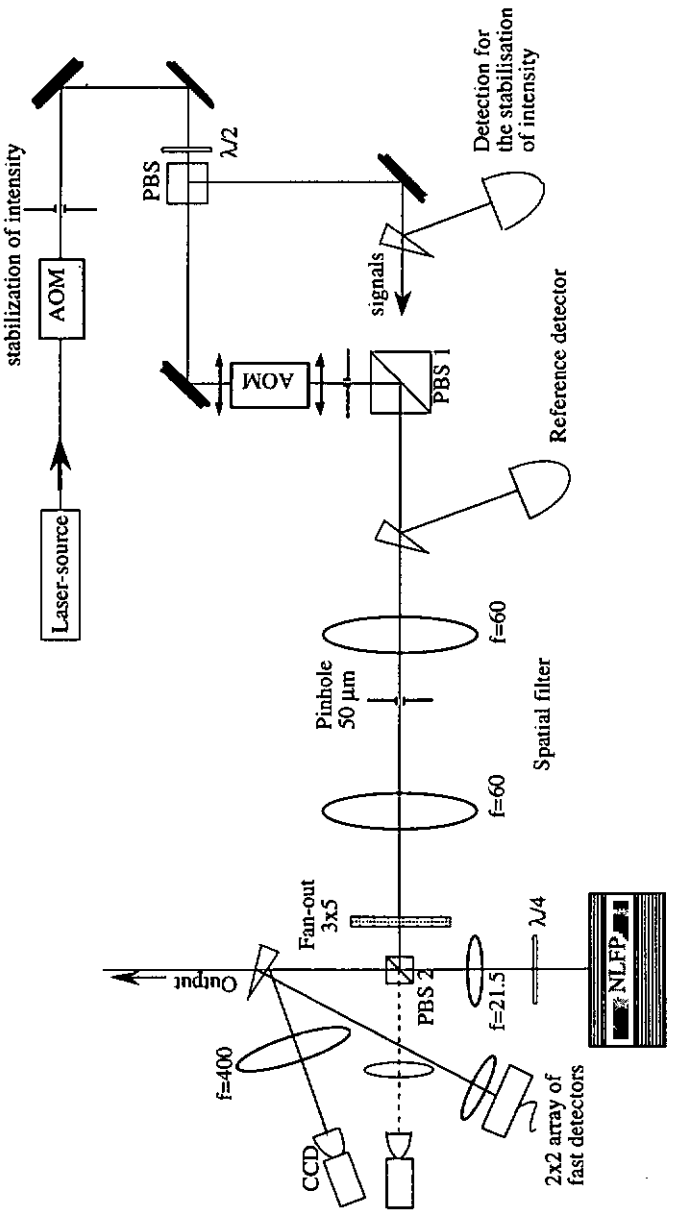


*Fig. 4-6 Experimental setup for the study of the NLFP in array format*

The output beams are reflected from an uncoated glass wedge and then detected on the CCD-camera. At the same time, a 2x2 array of fast detectors allows the detection of four of these output beams simultaneously by using the reflected beams on the second surface of the wedge.

The beams transmitted by PBS2 can serve to determine the characteristics of the fan-out element. We focus them on the CCD-camera by means of a lens of 500 mm focal length. For that purpose the polarization of the laser beam has to be rotated before PBS2 using a half-wave plate.

An incoherent illumination can be obtained on the sample by using the light of a 50 W halogen lamp injected in a fiber. This illumination serves to observe the sample surface which is imaged on the CCD-camera. A precise calibration of the distance on the surface is obtained using, as described in Chap. 2, the image of an USAF test target.

We find it convenient to initially adjust each part of the setup with the help of a He-Ne laser in place of the hold beam.

Figure 4-7 shows the part of the setup for the input of the 3x5 beams. The incidence of the beams is normal, since the fan-out element and the specimen are placed in the focal planes of the lens. The PBS2 is mounted on the same holder as the lens and the wave-plate. A fine adjustment is possible in x-y-z-$\theta$-$\varphi$ directions for all these elements together. The angles of the hold beams incident on the PBS2 are small and within the small angular range of this element ($\approx 8°$). It is necessary to use a sample-holder with fine adjustment capabilities for all directions and angles. This is a consequence of the focusing tolerance for the hold beam which is measured at less than 50 µm This is in agreement with the calculated Rayleigh range $z_0$ of 32 µm for a waist of 3 µm. The horizontal and the vertical positions are reproducibly determined by the computer controlled x-y table with an accuracy better than one motor step (2.5 µm). The temperature is stabilized better than 1.K with a Peltier element.

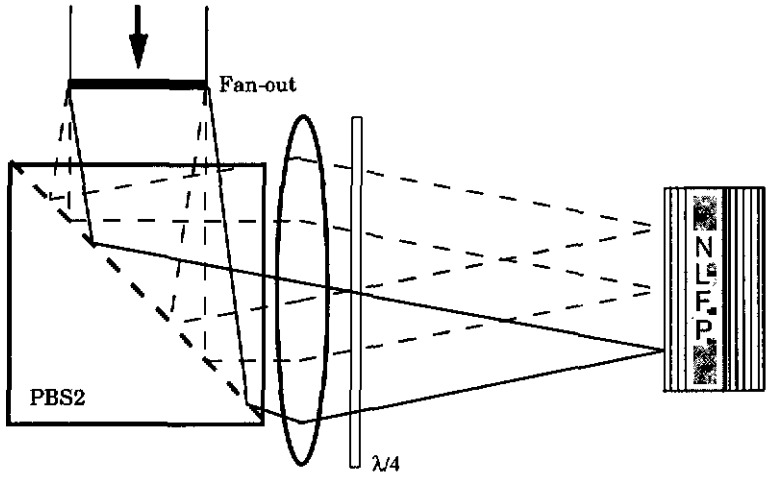


*Fig. 4-7 Enlarged diagram of the setup used to generate the 3x5 beams.*

## 4.4.3 Special parts in the setup

Some new parts in the setup merit a special attention :

THE FOURIER LENS (f = 21.5 mm)

A high quality lens has to be used to ensure hold spots of low aberration on the specimen. We use a doublet lens with a diameter of 6.5 mm (no vignetting) and a focal length of 21.5 mm at 885 nm. A calculated Strehl ratio of 0.96 for the on-axis and the off-axis beams demonstrates the negligible aberrations introduced by the lens. The quality of each spot of the array is verified on the CCD-camera.

DETECTION OF THE RESULTS : a) THE CCD-CAMERA

A high sensitivity CCD-camera (Pulnix, TM-36K) allows the detection with 8 bit resolution. Acquisition and data treatment are accomplished by using an acquisition card (Scion LG-3 frame grabber) and image processing software (Image 1.47) on a Macintosh. Each spot imaged on the camera is measured by approximately 30 x 30 pixels. But the maximum relative spectral response of the sensor is

limited to 15 % at $\lambda$ = 890 nm. This low spectral sensitivity is the main cause of error in the measurement of the uniformity for the fan-out element. The measured intensity values show a standard deviation of 4 %.

b) THE 2 X 2 DETECTORS ARRAY

The 2x2 detector array allows the simultaneous measurement of the switching characteristics of four NLFPs on a 4-channel oscilloscope. The detector array is fabricated at IMT. 4-segment Si-photodiodes (Hamamatsu S2856) and four fast settling wideband operational amplifiers (Burr-Brown OPA600, 5 GHz GBWP) are mounted in a transimpedance circuit, allowing high gain with 12 MHz bandwidth. Maximum risetime of 30 ns are obtained on the four detectors. It is possible to compare the switching dynamics of each NLFP of the 3x5 array by comparing four at a time.

INTENSITY STABILIZATION

We have developed the following system to reduce the intensity noise. A 40 MHz acousto-optic modulator (IntraAction Corp., Model AOM-40N) is placed at the output of the Ti:$Al_2O_3$ laser. It serves to decrease the intensity in the zero diffraction order if the laser intensity increases, and inversely if the laser intensity diminishes. A PI-regulator adjusts the power level of the AOM by regulating the amplification level of a large bandwidth preamplifier with respect to the difference of voltage between the signal measured by a photodetector placed in the setup (Fig. 4-6) and a constant voltage. A noise reduction from 2.4 % to 1.7 % is obtained. Although this reduction is small, it is useful for an accurate determination of the threshold powers in a NLFP array using the CCD-camera.

## 4.5 Operation in array format

### 4.5.1 Threshold uniformity of a 3x5 array of NLFPs : Measurement of the entity

We investigate the switching behavior of the 3x5 NLFPs in array format and we want to compare the measured threshold powers to those obtained with the single beam investigation of Sect. 4.3.2. The only change in the setup from the single beam investigation is to insert the Dammann fan-out element on a 1 mm glass plate, at a few millimeters before PBS2 (Fig. 4-6). The other parameters of the measurement are unchanged and the wavelength is the same. The two measurements are consecutive.

The threshold power of each NLFP is determined precisely with the observation of the switch-On on the CCD-camera (Fig. 4-3). The precision of the measurement is limited by the noise of the laser (less than 2 %) because the CCD-camera integrates the results during 40 ms. By increasing the power incident globally on the 3x5 devices with small steps, it is possible to measure the threshold power of each NLFP with the precision limited by the noise. We increase the global incident power by 0.2 mW steps. For each step we record the image of the 3x5 devices on the CCD-camera. From a global power of 24 mW where no NLFP is switched-On we increase the power to 27 mW where the 3x5 devices are switched-On in 14 steps. We can determine from the recorded images that the switch-On of all the NLFPs occurs between the third and the 11th acquisition, for a global power difference of 1.85 mW. The measurement is reported in Fig. 4-8. In the part a) (top), the 15 power measurements (14 power steps) from 24 to 27 mW detected by the reference detector are recorded on the digital oscilloscope, allowing the exact determination of the global incident power after each step. In Fig. 4-8 b)(bottom), the change in reflectivity of the five NLFPs of the central column of the array is reported, step by step.

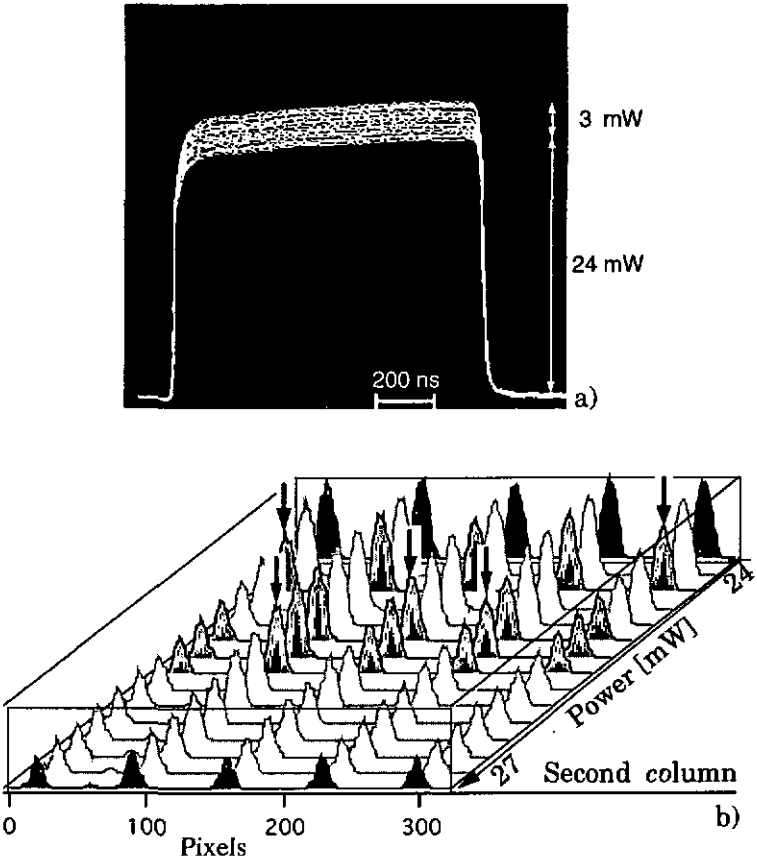


*Fig. 4-8* *a) The global power vs. time for 15 different incident global powers. The power difference ΔP = 3 mW, which is necessary to switch completely from Off- to On-state the 3x5 array of NLFPs, is indicated. This difference is divided in 14 steps (0.2 mW / step).*
*b) First line (24 mW) : Output intensity of five NLFPs in Off-state. Last line (27 mW) : Output intensity of the five NLFPs in On-state. In-between these lines, increase of the global power in 0.2 mW steps. Each NLFP at threshold is pointed out by an arrow.*

From the 24 mW incident power where all five NLFPs are in Off-state (back of the figure, element in high reflectivity state) to the 27 mW

where all the NLFPs are in On-state (front of the figure), the changes in reflectivity of each of the five elements are plotted with one plot for each power step. The important lines are evidenced in dark : first line (24 mW), last line (27 mW), and the lines where one element is at threshold (arrows).

From the measurements shown in Fig. 4-8 we can determine the threshold power of each NLFP element of the array. The results are reproduced in Fig. 4-9 in a similar form as for the measurements of Fig. 4-4.

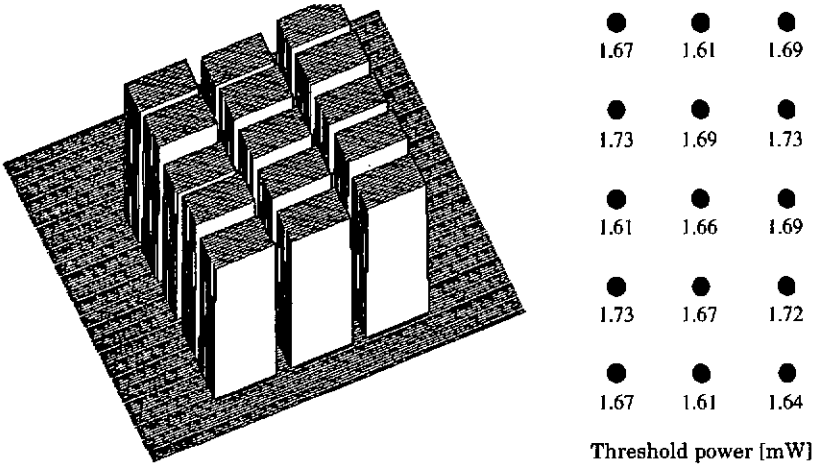


*Fig. 4-9 Measured threshold powers for each NLFP of the 3x5 array.*

We measure a mean threshold power of 1.68 mW. The 15 measured powers show a standard deviation of 2.5 % of this mean. In Sect. 4.3.2 we found threshold powers with a mean of 1.74 mW with a standard deviation of the mean power of 4.6 %. We can conclude that these two measurements are consistent. The mean power is expected to be lower for the array measurement due to a residual crosstalk.

### 4.5.2 Threshold uniformity of a 3x5 array of NLFPs : Dynamic measurements

The dynamic bistable switching of four NLFPs in the array can be measured simultaneously by measuring the output power of the

devices by means of the 2x2 fast detector array and a four channel oscilloscope. Fig. 4-10 shows the oscilloscope traces representing the switch-On of the four NLFPs in the bottom right of the array in Fig. 4-9. The threshold powers are increased to about 2 mW pro device because the spectral detuning from the resonance minimum is set higher than for the previous measurements ($\lambda$ = 888.61 nm compared to 888.76 nm before). The exact situation on the sample where the above measurements were made is not recovered exactly, since the optical elements were realigned. Therefore these measurements cannot be compared directly with those above.

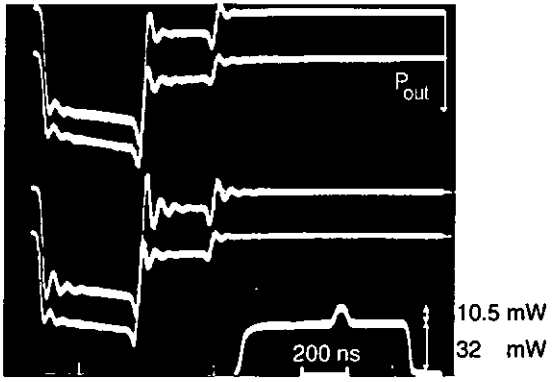


*Fig. 4-10 Fast (simultaneous) latched switching of four NLFPs on sample #487 : Output power vs. time of the four devices detected with a fast 2x2 detector array (risetime ≈ 30 ns). The input pulse measured in global power on the reference detector is traced at the bottom right of the picture.*

We use the detector array to determine the threshold powers of the NLFPs of the 3x5 array. The global incident power is increased following a positive ramp of 70 mW in 500 ns. We use this slow, linear power increase to compare the switching time of each element in the array. The switching time difference is measured between each device which switches. It is converted into a switching power difference by multiplying by the gradient of the ramp. This comparison of the switching time is made two by two with the elements. The threshold power of each element is calculated. The results are shown in the Fig. 4-11. The mean threshold power for the 3x5 NLFPs is 1.96 mW.

The standard deviation is of 9.5 % of the mean threshold power for the 3x5 elements. The standard deviation determined with this method tends to be increased by the comparison of the switching times two by two and by the long time needed for the total measurement. Nevertheless for the dynamic switching measurement of four devices only, the use of the detector array seems adequate. The error in the comparison of the switching time for 4 NLFPs is estimated small, because the four detectors show similar characteristics. This time error is estimated at ± 4 ns, corresponding to an error in power of ± 2 % for one device.

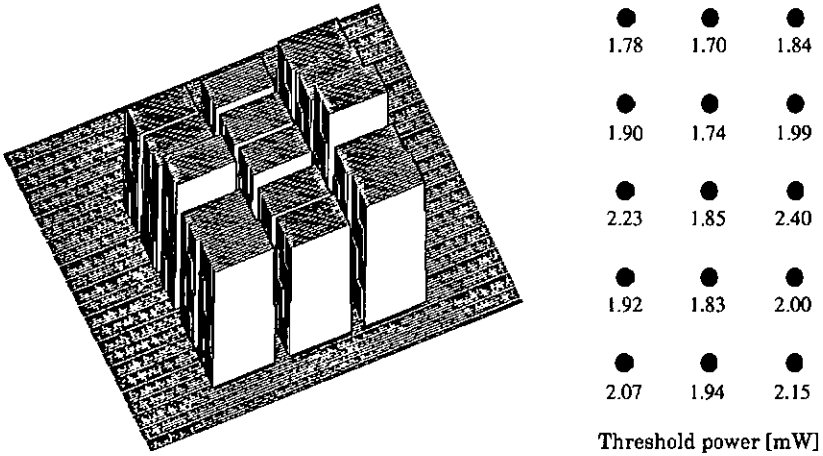


*Fig. 4-11 Threshold powers of 3x5 NLFPs in array format measured by comparison of dynamic switching times.*

## 4.6 Conclusion

### 4.6.1 Summary

The present measurements on array operation are conducted on a surface of 0.02 $mm^2$ in the low gradient zone of sample #487. Typical threshold power of 1.74 ± 0.08 mW and switching contrast from 3:1 to 4:1 are determined. A Dammann grating is used to generate the 15

beams for the 3X5 array of devices. The grating shows an uniformity better than 10 % and an efficiency of 80 %. In the array, each NLFP is separated from the other with a spacing of 50 μm. This spacing limits the crosstalk between the spots to less than about 5 % for the threshold power.

A setup is built for the operation of the NLFP in array format. We use a CCD-camera for detection and image acquisition software. The CCD-camera is not an efficient means to measure the characteristics of the fan-out element, because the power detection is only achieved with ± 4 % of precision. Nevertheless it is suitable to determine the change in reflectivity of imaged NLFPs (the precision of the determination is limited by the ± 2 % noise of the laser).

We have found an area on sample #487 which can be used for array operations. The switching characteristics of this array of NLFP are measured using the CCD-camera. By increasing the global incident power on the 3x5 NLFPs from 24 to 27 mW, all the devices can be switched-On from high to low reflectivity state. The threshold powers of the 3x5 devices are measured in the range of 1.68 ± 0.06 mW. The dynamic switching characteristics of the NLFPs of the array are also measured using a 2x2 fast detector array for the output beams detection.

## 4.6.2 Discussion

CONSEQUENCES FROM THE MEASUREMENTS IN ARRAY FORMAT

Since Jewell et al. [29] first reported the parallel operation of optical logic étalons in GaAs, there has been, to our knowledge, no measurement of the threshold power uniformity on NLFP in an array format.

We observe a correspondence between the threshold powers measured sequentially for each NLFP used in the array (4.3.2) and those measured in array format with the CCD-camera (4.5.1). We conclude that the threshold power uniformity is determined by the sample homogeneity and not by the uniformity of the fan-out grating. The threshold power uniformity is limited to ± 4.6 % by this homogeneity. We have seen in Fig. 4-2 that the sample

inhomogeneity is determined by the quality of the crystal growth rather than by the thickness gradient. Moreover, we believe that this inhomogeneity recorded over 100 μm does not get worse over 1 mm. The excellent thickness gradient will allow us to use larger areas on the sample, if more hold power is available. We estimate an error of more than ± 2 % in the threshold power determination for the sequential case (due to threshold and displacement uncertainties). However, in the array format case, the error of less than ± 2 % is due to the noise of the laser.

There are further consequences of the measured wafer inhomogeneity. The nonuniformity in the threshold power increases the switching window ΔP (3.1.1). ΔP is estimated to be less than 11 %·$P_{th}$ assuming a threshold power nonuniformity of 9.2 % and a laser noise of 1.7 %. The enlarged switching window ΔP leads to a reduction of the achievable differential gain in the NLFP from 10 (3.1.2) to 4.5. In a high contrast regime, a small array of NLFPs cannot be accommodated with a fan-in and a fan-out of two in a NOR-gate configuration for a switching window ΔP = 11 %·$P_{th}$ (worst case). Only a maximum enlarged switching window of 9.1 %·$P_{th}$ could be accommodated with this fan-in and fan-out of two, and the general switching condition for the NLFP (equations developed in Sect. 3.1.1 for the worst case, we used $r_L$ = 0.5 in the calculations).

MAXIMUM SIZE OF THE ARRAY ON SAMPLE #487

We measured a wavelength change of 2 nm for a 10 mm diameter disk at the center of the sample (0.4 % thickness change for 5 mm) (4.3.1). A change in resonance wavelength of 0.1 nm induces a change of about 10 % in the threshold power (the threshold power increases as 1 mW/nm 2.2.3). Therefore, the same threshold power within the tolerance can be found on a 0.5 mm diameter disk at the center. A spot spacing of 50 μm between the devices leads to a possible utilization of about 80 NLFPs using the same wavelength on the sample #487.

Instead of 80 devices with 50 μm spacing between each, about 2000 NLFPs could be used with the same tolerance and on the same device using pixellation. Pixellation allows one to reduce the spacing between the devices to less than 10 μm as demonstrated in refs.

[27, 28]. The use in parallel of 2000 devices will create difficulties with regard to the power required from the source (3 W), and the heat to be removed from the sample (1.5 $kW/cm^2$).

# 5 Conclusion

THE NLFP DEVICE

The structure of the nonlinear Fabry-Perot device (NLFP) consists of a 2 μm nonlinear spacer in GaAs sandwiched between two AlGaAs mirrors. The design of this structure shows that the thickness of the spacer is critical for good performance. For example, the resonance wavelength must be within ± 3 nm of the design wavelength, in order to maintain approximate impedance match and thus to achieve good contrast. The design wavelength is chosen at 885 nm which is the average of a range of wavelengths where the threshold is minimum. Therefore the accuracy of the growth for the spacer length must be better than 0.5 %.

The structures of the nonlinear Fabry-Perot devices were grown by molecular beam epitaxy at the Institut de Micro- et Optoélectronique of the Ecole Polytechnique Fédérale in Lausanne. Two structures showed spacer accuracies of 1 and 2 %. Therefore, although they could be used, the contrast was not optimal. Three NLFPs demonstrated bistable features. Typical threshold power of 1.5 mW and switching contrast varying from 3.5 to 8:1 (impedance matched) were measured. Bistability was observed at wavelengths between 853 and 890 nm using the same NLFP sample. Different positions on the wafer were used for the bistability measurements at wavelengths from 860 to 890 nm. We used the next higher order of resonance to measure the bistability from 853 to 860 nm (see Annex).

THE DEVICE TOWARDS ITS OPERATION IN ARRAY FORMAT

We built a setup which allows nonlinear spectral reflectivity measurements and dynamic switching measurements for two- and three-port operations. The setup allows the normal incidence of the hold beam and either the normal or the off-axis incidence of the signal beam. The NLFP has been used in two-port operation with a

differential gain up to 7. Three-port operation with a differential gain of more than 5 has been shown at high duty cycle.

Off-axis address has been investigated with the following result. In agreement with the theory, there is a tendency for the signal beam power necessary to switch-On the device to decrease at angles between 6° and 10°, for a constant hold beam. Moreover, the angle of 10° allows the addressing of two signal beams with the same polarization on the NLFP with negligible interference effects. The hold beam, with an orthogonal polarization to the signals, must remain on-axis to avoid a loss of finesse. The spatial fan-in of the NLFP using a 6 μm spotsize hold beam is limited to 2. However it can be increased for larger hold beam diameters using the switching wave phenomenon. Two distant diffraction limited signal spots can be coupled by increasing the spotsize of the hold beam. However, this entails an increase of the energy necessary for switching-On the device and a slower switching time. Diffusion also couples two distant hold beams. A spacing of 50 μm between the elements of an array of NLFPs has been found necessary to reduce the crosstalk between two devices to less than 1 %, for the case of optical pixellation.

The NLFP has been used in cascadable operations, which are limited by a gain-bandwidth product of about 100 MHz.

## OPERATIONS IN ARRAY FORMAT

We extended the setup by using a Dammann grating to generate a 3x5 array of spots on the sample. In addition, we used a CCD-camera to allow the accurate measurement of array switching and a fast detector array to observe the dynamic switching of four NLFPs. The whole array is switched from high to low reflectivity state with the addition of 3 mW to a global incident power of 24 mW.

The sample homogeneity limits the threshold power uniformity across the array using a single beam to ±4.6 %. This uniformity is no worse when the fan-out element is used to generate the array. This inhomogeneity is determined by the quality of the crystal growth rather than by the thickness gradient of the sample, which is less than 0.3 % thickness change for a 10 mm diameter disk at the center. We estimate the causes of this nonuniformity in threshold power first to small inhomogeneities or dust at the surface of the sample, which

reduce the coupling of the light into the cavity. However, every precaution was taken to keep the sample clean. A second cause can be the local change in the recombination time $\tau$ induced by recombination centers in the structure.

## THE NLFP USED AS A PARALLEL PROCESSING DEVICE IN AN ADVANCED SYSTEM

The consequence of the threshold power nonuniformity of ±4.6 % for the switching conditions of the NLFP in a cascadable system is to increase the switching window to 11 %·$P_{th}$. The increased switching window limits the achievable gain for an array of NLFPs to 4.5. In the worst case, the switching window prohibits the two-port operation of a NLFP to a fan-in and a fan-out of two (maximum switching window = 9.1%·$P_{th}$).

It is advantageous to use rather the three-port characteristic of the NLFP which shows almost constant power in the Off-state. This characteristic is more tolerant because the reflected signals do not add to the output beam. In the worst case, a maximum switching window of 9.7 %·$P_{th}$ is allowed (74 %·$P_{th} \leq P_{Hold} \leq$ 77 %·$P_{th}$ and 30 % ≤ A ≤ 40 %; where A is the maximum loss factor which can be allowed between successive gates).

The NLFP suffers from some constraints. On the device level, it has a critical biasing requirement, and critical slowing down effects limit the gain achievable. A wavelength stability of ≤ 0.1 nm and a temperature stability of ≤ 0.5 K are required [1]. On the array level, it is limited by sample inhomogeneity. We can conclude that the use of the NLFP as a parallel processing element in an advanced cascadable system is critical.

# Annex

## A1 The NLFP used in a modified regime

### A1.1 Introduction

The usual distinction between bistable devices using either the absorptive or the dispersive nonlinear effect is clearly not strictly valid, since the nonlinear refractive index change and the absorption are related through the Kramers-Kronig transform and the use of one without a small contribution of the other is not possible. Till now, we showed in this work a NLFP device where the effects of nonlinear refraction predominate and a small change in the refractive index can give bistability by the use of a high finesse resonator. We want to show that the combination of the absorptive and dispersive nonlinearities lead to a new type of bistable device. The energy of the incident photon is above the gap.

The first part includes the nonlinear spectral reflectivity measurements (SRM) at photon energies above the gap. These spectra are compared with simulations. In a second part, the dynamic measurements of the NLFP in a modified regime (above the gap) are presented. In a third part, the changes of the nonlinear refractive index and of the absorption at different light intensities are evaluated for different photon energies above (and below) the gap.

### A1.2 Nonlinear spectral reflectivity measurements of optical bistability above the gap

We measure the optical bistable switching of the NLFP device, which is switched-On using the incident light at photon energies above the gap. The device uses a Fabry-Perot resonance in the spectral range at shorter wavelengths (i.e. a higher resonance order). For the sample

#487, the resonance at $\lambda = 857$ nm is found near the center of rotation. The corresponding spectral reflectivity measurement (SRM) using pulses of 1 μs duration with a duty cycle 100:1 is shown in Fig. A1-1. This resonance has only a very low finesse for small incident power (solid line in Fig. A1-1), since the back mirror is masked by the high absorption cavity. Figure A1-1 demonstrates that for incident power increasing from 60 μW to 61 mW the finesse increases and the resonance is shifted towards shorter wavelengths. Optical bistability is observed at 61 mW by a jump from high to low reflectivity and a quasi-infinite differential reflectivity at $\lambda = 853$ nm (dots represent the measured points). The finesse of the resonance increases in this case from less than 2 at low power to more than 9 at 61 mW. Optical bistability with a lower reflectivity change is observed for a power below 61 mW.

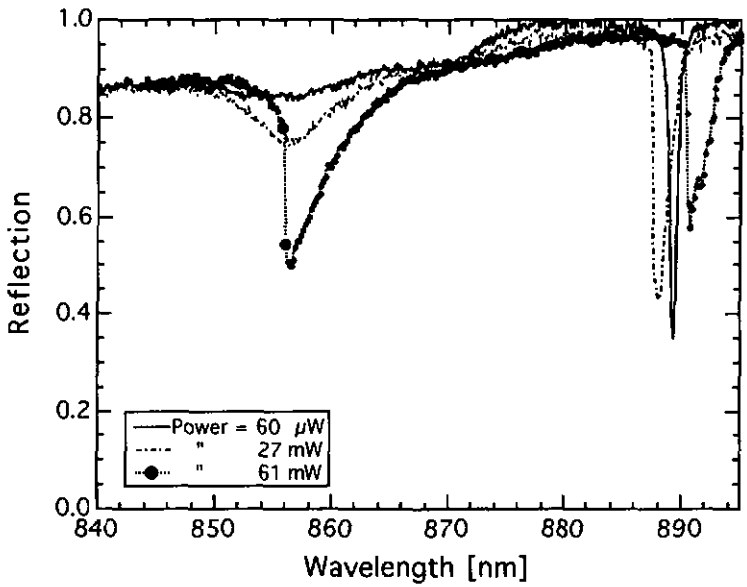


*Fig. A1-1 SRM for incident powers of 60 μW, 27 mW and 61 mW on a 6 μm spotsize on sample #487. The powers are measured at $\lambda = 852$ nm.*

The results of more detailed measurements of the spectral reflectivity at different wavelengths are shown in Fig. A1-2. For wavelengths corresponding to energies above the gap, optical bistability is found for 55 and 61 mW of incident power. The behavior of the change of the resonance wavelength for different incident powers is indicated in Fig. A1-2 by a solid line with an arrow indicting the direction for increasing power. This change is initially up to 11 mW towards higher wavelengths. The same behavior was found in simulation using plane waves up to power levels of 30 mW.

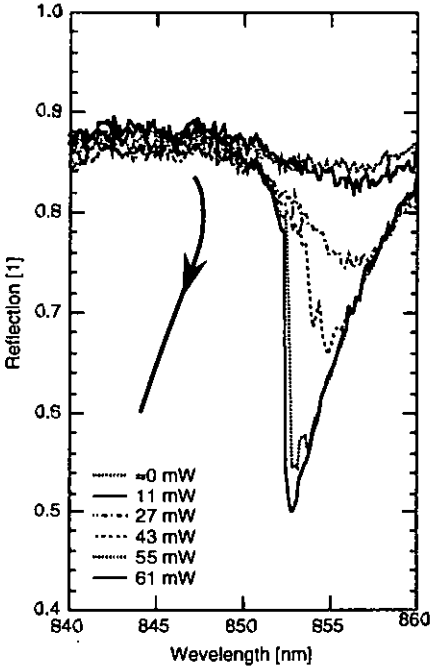


*Fig. A1-2 SRMs for incident powers from 60 μW to 61 mW on a 6 μm spotsize on sample #487. The change in the resonance wavelength is sketched at the left of the figure.*

The observed decrease in the absorption $\alpha(\lambda,I)$ for an increasing incident power is in agreement with the measurements of Lee et al. [10] (Fig. 2-1). Equally, the observed movement of the resonance wavelength (first right then left) is consistent with Lee's measurements of refractive index change in this wavelength regime.

## A1.3 Dynamic switching measurements

Figure A1-3 shows bistable switching above the gap ($\lambda \approx 853$ nm) at high incident power. A 55 mW power beam, to which a short pulse (100 ns) of 12 mW is added, induces latched switching which lasts for more than 300 ns. The switch-Off is caused by the positive refractive index change induced by heating. The measured contrast at switch-On is 3.5:1. Switch-On time is detector limited (10-20 ns).

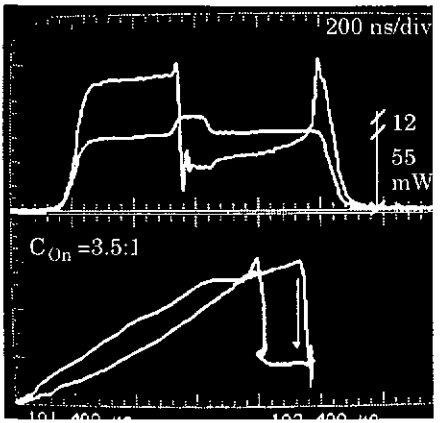


*Fig. A1-3 Bistable (latched) switching above the gap on sample #487. Top : power of input and output beams vs. time. Bottom : output power vs. input power. The hysteresis is traversed in the clockwise direction.*

A power of 90 mW incident on a NLFP in a high absorption regime (wavelength far below 870 nm) induces a strong heating, the effects of which are shown in Fig. A1-4. The wavelength is shifted by 0.6 nm from the first pulse to the second one. The figure shows the changes in reflectivity of the sample which are caused by the motions of the resonance (sketch on the top of the figure). These motions are due to the positive change in refractive index induced by heating. The first part of the pulse switches the NLFP On to its low reflectivity state. Then heating will switch it slowly Off. The contrast at switch-On is 2.6 : 1. The wavelength detuning from the resonance minimum is smaller for the second pulse. The incident power is the same. At switch-On the NLFP will first reach the minimum reflectivity state,

and then increase again the reflectivity by moving to the high wavelength side of the resonance. The low reflectivity state (resonance minimum) is recovered at the middle of the pulse duration due to heating.

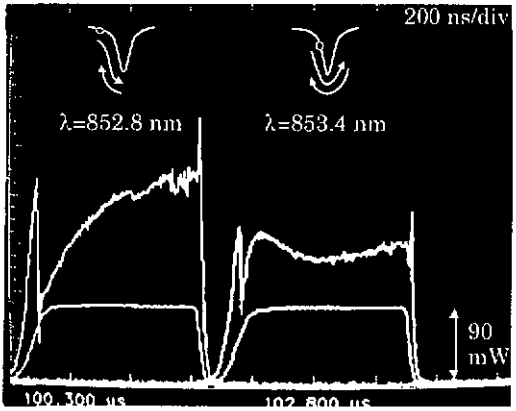


*Fig. A1-4 Incident and reflected power vs. time for two pulses at different wavelengths (852.8 nm and 853.4 nm) on sample #487. The thermally induced motion of the resonance during the pulse (λ is constant) is sketched at the top of the figure.*

This unusual switching characteristic is only found well above the gap. Just above the gap (λ = 870 nm) we find a characteristic similar to the switching below gap, as in Fig. 2-10. The switching characteristic for this case is shown in Fig. A1-5. Here, the incident power is 45 mW instead of 1.6 mW in the case below the gap. Switch-On time is detector limited (10 ns). The measured contrast is more than 4:1. (The decrease of the reflectivity in On-state during the whole pulse is due to the non-square pulse generated by the pulse generator.)

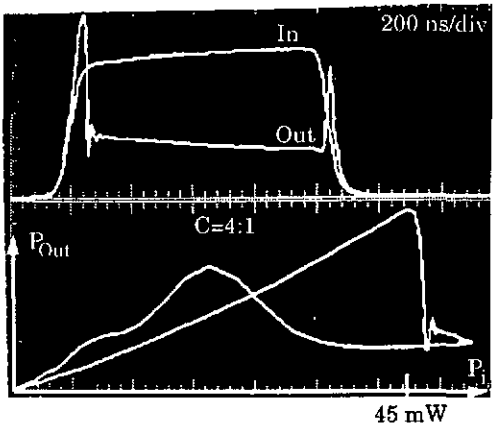


*Fig. A1-5 High contrast bistable switching characteristics at photon energy just above the gap ($\lambda$ = 870 nm) on sample #487. Up : incident and reflected power vs. time. Down : corresponding hysteresis plot traversed in the clockwise direction.*

## A1.4 Absorption and refractive index change investigated above the gap

We determine the absorption and the refractive index variations for different incident powers of the laser beam (0 to 15 mW) and different operating wavelengths (847 to 867 nm). The values are deduced from nonlinear SRM. Absorption is determined from the reflectivity measured at the resonance minimum (Eq. (2-10)). A fit of this relation to the SRM allows the precise determination of the parameter $\rho$ and consequently of the absorption at resonance minimum (Eq. (2-7)). The wavelength of the minimum of the low finesse resonance is also precisely determined from the fit. A small wavelength range around the minimum is used for the fit (typically 6.5 nm corresponding to 35 measured points). The variations of the nonlinear refractive index with respect to the incident intensity are deduced from the changes of the wavelength of the resonance minimum for different nonlinear SRMs. The method to determine the nonlinear refractive indices from SRMs is proposed in Ref. [7]. The measurements are conducted on

sample #337. The wavelength of the resonance is varied by choosing different places of investigation on the sample. The spotsize of the incident beam is adjusted to 12 μm to reduce the effects of the carrier diffusion. Figure A1-6 shows the changes of the absorption $\alpha(\lambda,I)$ and of the refractive index $\Delta n(\lambda,I)$ with respect to the changes of incident power for different wavelengths.

The absorption falls off linearly with increasing incident power, at different rates for different wavelengths. It is also in an absolute sense about 40 % lower than the measurements of Lee et al. [10] (Fig. 2-1). The refractive index change varies in a more complicated manner. At all wavelengths measured, there is a positive gradient with respect to increasing power at low incident power. This shifts the resonance to longer wavelengths. At higher incident powers the gradient becomes negative. However, the power at which this occurs depends on the wavelength. Close to the gap, this occurs at relatively low power. Two such cases are shown in the Fig. A1-6 ($\lambda$ = 864 and 866.7 nm). This negative gradient shifts the resonance to shorter wavelengths. This measurement provides an understanding for the behavior of the resonance wavelength in Fig. A1-2. The determined $\Delta n$-changes are in agreement with the data of ref. [10] (Fig. 2-1).

We can determine the internal intensity I into the cavity of the NLFP from the incident intensity $I_i$, the reflectivity of the device R, and the absorption following the relation

$$I = I_i \frac{1-R}{\alpha L}. \qquad \text{(A1-1)}$$

where L is the length of spacer. This relation is obtained from spatially averaging the intensity in the cavity and Eq. (2-10). The formula is developed for a low finesse cavity where the approximation of Eq. (2-14) is not available.

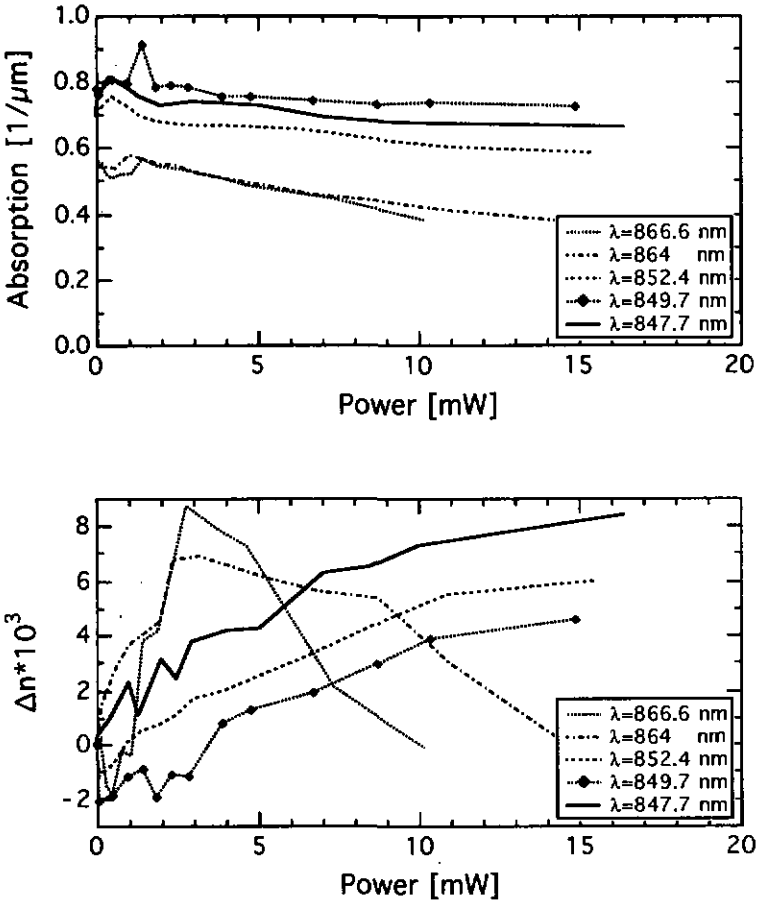


*Fig. A1-6 Changes in absorption (top) and in the refractive index (bottom) with respect to the incident power on a 12 μm spotsize. The points are determined from nonlinear SRMs at photon energies above the gap on the sample #337. The number of points indicated for λ = 849.7 nm is the number of SRMs used to get the curve.*

We have calculated the slopes of all the absorption curves and two of the refractive index curves above 2.5 mW versus the internal intensity. The slopes $\tilde{\alpha}_2$ and $\tilde{n}_2$ are presented in Table A.1.

| Wavelength [nm] | $\alpha_0$ [$\mu m^{-1}$] | $\tilde{\alpha}_2$ [$\mu m/mW$] | $\tilde{n}_2$ [$\mu m^2/mW$] |
|---|---|---|---|
| 847.7 | 0.75 | 3.55 | |
| 849.7 | 0.75 | 3.25 | |
| 852.4 | 0.72 | 3.22 | |
| 864 | 0.55 | 3.99 | - 0.128 |
| 866.6 | 0.55 | 4.28 | - 0.265 |

*Table A.1 Phenomenological coefficients $\tilde{\alpha}_2$ and $\tilde{n}_2$ characterizing the linear absorption and refractive index change at different wavelengths with respect to the internal intensity in the cavity of the sample #337.*

The determined phenomenological coefficient $\tilde{n}_2 \approx -2 \cdot 10^{-3}$ cm²/kW is 30 times higher than the phenomenological Kerr coefficient $n_2 \approx -7 \cdot 10^{-5}$ cm²/kW determined for a photon energy below the gap (2.2.4). This is related to the 30 times higher absorption of $7 \cdot 10^3$ $cm^{-1}$ measured above the gap in comparison to $\alpha = 250$ $cm^{-1}$ below the gap.

## A1.5 Conclusion

We have presented spectral reflectivity measurements and dynamic measurements for photon energies above the gap of bulk GaAs. We observed some characteristics of physical interest. A type of bistability has been found which combines mixed absorptive and dispersive effects. It was observed on sample #487 at wavelengths between 850 nm and 870 nm (wavelength of the gap). The power of switch-On is high (more than 40 mW). When the power is increased to 60 mW, the finesse of the resonance at 853 nm increases from less than 2 to more than 9. The finesse increase is due to the decrease of absorption. This is predicted by the plasma theory [11]. In addition, we observed a shift of the resonance wavelength in agreement with the predicted behavior of the refractive index changes.

Dynamic measurements are conducted at wavelengths of 853 and 870 nm. A latched bistable switching is observed during more than 300 ns at 853 nm with a switch-Off caused by thermal effects. A bistable switching with a contrast of more than 4 : 1 is measured at $\lambda = 870$ nm for an incident power of 45 mW.

The absorption and the refractive index changes are determined for different powers from 0 to 15 mW by fitting the theoretical reflection model on the results of nonlinear SRMs measured on sample #337. The absorption data are directly obtained from the fit and the nonlinear refractive index change is calculated. Five different resonance wavelengths from 848 to 867 nm are investigated. Phenomenological material coefficients $\tilde{\alpha}_2$ =350 cm/kW and $\tilde{n}_2 = -2 \cdot 10^{-3}$ cm$^2$/kW are determined. $\tilde{n}_2$ is 30 times higher than the phenomenological Kerr coefficient $n_2$ determined at photons energies below the gap ($n_2 = -7 \cdot 10^{-5}$ cm$^2$/kW). This is related to the 30 times higher absorption of $7 \cdot 10^3$ cm$^{-1}$ measured above the gap compared with $\alpha = 250$ cm$^{-1}$ below the gap.

# Acknowledgements

First, I want to express my gratitude to the director of my thesis, Prof. René Dändliker, for his support and his encouragement. I fully appreciated his remarkable competence and knowledge.

Special thanks go to Dr. Bruno Acklin and Dr. Neil Collings for their motivating help during four years of pleasant collaboration. I benefited highly of their suggestions and ideas.

I intend to thank the members of the jury, Prof. Brian S. Wherrett, Prof. Arvind Shah and Dr. Jean-Louis Oudar for their interest in my thesis work and for their constructive advises.

I want to thank Dr. Marc-André Dupertuis for welcoming me at IMO-EPFL and for his availability.

Finally, I am grateful to my colleagues who create with their kindness, their sympathy and their disponibility a very pleasant atmosphere for working at IMT-Uni-Ne, and to my family and to Jeanne-Marie Visconti for their presence which made me happy.

This work was supported by the Swiss National Science Foundation (grants 4.045-0.87.13 and 21-30105.90)

# References


1. B. Acklin, "Bistable GaAs Fabry-Perot and Bragg reflector devices for optical computing," Ph. D. thesis, University of Neuchâtel, Switzerland (1992).
2. H. M. Gibbs, S. L. McCall, T. N. C. Venkatesan, A. C. Gossard, A. Passner and W. Wiegmann, "Optical bistability in semiconductors," Appl. Phys. Lett. **35**, 451 (1979).
3. H. M. Gibbs, J. L. Jewell, J. V. Moloney, M. C. Rushford, S. S. Tarng, K.Tai, E. A. Watson, A. C. Gossard, S. L. McCall, A. Passner, T. N. C. Venkatesan and W. Wiegmann, "Switching of a GaAs bistable etalon: external switching on and off, regenerative pulsations, transverse effects and lasing," Proc. SPIE **321**, 67 (1982).
4. B. Acklin, C. Bagnoud, M. A. Dupertuis, D. Martin and F. Morier-Genoud, "Low-threshold optical bistability in bulk GaAs etalons," OSA Proceedings on Photonic Switching, vol. 8, H. Scott Hinton and Joseph W. Goodman, eds., (Optical Society of America, Washington, DC, 1991) p. 231.
5. B. Acklin, C. Bagnoud, M. A. Dupertuis, M. Proctor, F. Morier-Genoud and D. Martin, "Thermally stable operation of a bistable Fabry-Perot etalon with a bulk GaAs spacer," Appl. Phys. Lett. **60**, 3099 (1992).
6. T. Sanada, S. Yamakoshi, O. Wada, T. Fujii, T. Sakurai and M. Sasaki, "Monolithic integration of an AlGaAs/GaAs multiquantum well laser and GaAs MESFETs on a semiinsulating GaAs substrate by Molecular Beam Epitaxy," Appl. Phys. Lett. **44**, 325 (1984).
7. B. G. Sfez, J. L. Oudar, J. C. Michel, R. Kuszelevicz and R. Azoulay, "High contrast multiple quantum well optical bistable device with integrated Bragg reflectors," Appl. Phys. Lett **57**, 324 (1990).

8. A. Miller, R. J. Manning, P. K. Milsom, D. C. Hutchings, D. W. Crust and K. Woodbridge, "Transient grating studies of excitonic optical nonlinearities in GaAs/AlGaAs multiple-quantum-well structures," J. Opt. Soc. Am. B **6**, 567 (1989).

9. H. Haug and S. W. Koch, "Quantum theory of the optical and electronic properties of semiconductors," World Scientific, Singapoore (1990).

10. Y. H. Lee, A. Chavez-Pirson, S. W. Koch, H. M. Gibbs, S. H. Park, J. Morhange, A. Jeffrey, N. Peyghambarian, L. Banyai, A. C. Gossard and W. Wiegmann, "Room-temperature optical nonlinearities in GaAs," Phys. Rev. Lett. **57**, 2446 (1986).

11. L. Bányai and S. W. Koch, "A simple theory for the effects of plasma screening on the optical spectra of highly excited semiconductors," Z. Phys. B - Condensed Matter **63**, 283 (1986).

12. D. E. Aspnes, "Table of optical functions of intrinsic GaAs: refractive index and absorption coefficient vs energy (0-155 eV)," EMIS Datareview RN=15437, (1985).

13. H. Kressel and J. K. Butler, "Semiconductor lasers and heterojunction LEDs," Academic Press, New York (1977).

14. B. S. Wherrett, "Fabry-Perot bistable cavity optimization on reflection," IEEE J. Quantum Electron. **QE-20**, 646 (1984).

15. B. G. Sfez, R. Kuszelewicz, J. L. Oudar, "Measurement of the nonlinear refractive index of semiconductors included in monolithic étalons," Opt. Lett. **16**, 855 (1991).

16. R. Bonifacio and L. A. Lugiato, "Cooperative effects and bistability for resonance fluorescence," Opt. Commun. **19**, 172 (1976).

17. B. Acklin, N. Collings and C. Bagnoud, "Criteria for the use of nonlinear GaAs etalons for threshold logic," Esprit workshop on Information Technology, Heriot-Watt University, Edinburgh, Scotland, (1991).

18. B. G. Sfez, "Bistabilité optique dans des micro-résonateurs à multi-puits quantiques," Ph. D. thesis, Orsay, France (1991).

19. E. Garmire, "Criteria for optical bistability in a lossy saturating Fabry- Perot," IEEE J. Quantum Electron. **QE-25**, 289 (1989).

20. M. E. Prise, N. Streibl and M. M. Downs, "Optical conaiderations in the design of digital optical computers," Opt. and Quantum Electron. **20**, 49 (1988).

21. C. Bagnoud, B. Acklin and N. Collings, "Use of bistable GaAs Fabry-Perot devices as all-optical logic gates," Topical meeting on Photonic Switching, A.M Goncharenko, F.V. Karpushko, G.V. Sinitsyn, S.P. Apanasevich, eds., Proc. SPIE vol. 1807, p. 201 (1992).

22. N. N. Rozanov, "Hysteresis phenomena in distributed optical systems," Sov. Phys. JETP **53**, 47 (1981).

23. B. G. Sfez, R. Padjen and J. L. Oudar, "Experimental evidence of hyateresis narrowing due to carrier diffusion in optical bistable etalons," QELS 91, Vol. 11, paper QTul34, Technical Digest Series, (Optical Society of America, Washington DC, 1991), p. 96.

24. R. Jin, D. Richardson, S. W. Koch and H. M. Gibbs, "Enhancement of differential gain of GaAs etalons by angle tuning of the switch beam," Opt. Eng. 28, 344 (1989).

25. S. D. Smith, "Optical bistability, photonic logic, and optical computation," Appl. Opt. **25**, 1550 (1986).

26. H. S. Hinton, "Architectural considerations for photonic switching networks," IEEE J. Select. Areas Commun. **SAC-6**, 1209 (1988).

27. T. Rivera, F. R. Ladan, A. Izraël, R. Azoulay, R. Kuszelewicz and J. L. Oudar, "Reduced threshold all-optical bistability in etched quantum well microresonators," European Quantum Electronics Conference, Florenz, (1993).

28. B. G. Sfez, E. V. Rao, Y. I. Niasim and J. L. Oudar, "Operation of nonlinear GaAs/AlGaAs multiple quantum well microresonatora fabricated using alloy mixing techniques," Appl. Phys. Lett. **60**, 607 (1992).

29. J. L. Jewell, Y. H. Lee, J. F. Duffy, A. C. Gossard and W. Wiegmann, "Parallel operation and crosstalk measurements in GaAs étalon optical logic devicea," Appl. Phya. Lett. **48**, 1342 (1986).

30. W. J. Firth and I. Galbraith, "Diffusive transverse coupling of bistable elements - switching waves and crosstalk," IEEE J. Quantum Electron. **QE-21**, 1399 (1985).